

# Techniques for blood volume fMRI with VASO

Citation for published version (APA):

Huber, L., Ivanov, D., Handwerker, D. A., Marrett, S., Guidi, M., Uludağ, K., Bandettini, P. A., & Poser, B. A. (2018). Techniques for blood volume fMRI with VASO: From low-resolution mapping towards sub-millimeter layer-dependent applications. *Neuroimage*, *164*, 131-143. <https://doi.org/10.1016/j.neuroimage.2016.11.039>

## Document status and date:

Published: 01/01/2018

## DOI:

[10.1016/j.neuroimage.2016.11.039](https://doi.org/10.1016/j.neuroimage.2016.11.039)

## Document Version:

Accepted author manuscript (Peer reviewed / editorial board version)

## Document license:

CC BY-NC-ND

## Please check the document version of this publication:

- A submitted manuscript is the version of the article upon submission and before peer-review. There can be important differences between the submitted version and the official published version of record. People interested in the research are advised to contact the author for the final version of the publication, or visit the DOI to the publisher's website.
- The final author version and the galley proof are versions of the publication after peer review.
- The final published version features the final layout of the paper including the volume, issue and page numbers.

[Link to publication](#)

## General rights

Copyright and moral rights for the publications made accessible in the public portal are retained by the authors and/or other copyright owners and it is a condition of accessing publications that users recognise and abide by the legal requirements associated with these rights.

- Users may download and print one copy of any publication from the public portal for the purpose of private study or research.
- You may not further distribute the material or use it for any profit-making activity or commercial gain
- You may freely distribute the URL identifying the publication in the public portal.

If the publication is distributed under the terms of Article 25fa of the Dutch Copyright Act, indicated by the "Taverne" license above, please follow below link for the End User Agreement:

[www.umlib.nl/taverne-license](http://www.umlib.nl/taverne-license)

## Take down policy

If you believe that this document breaches copyright please contact us at:

[repository@maastrichtuniversity.nl](mailto:repository@maastrichtuniversity.nl)

providing details and we will investigate your claim.

This work is licensed under the Creative Commons Attribution-NonCommercial-NoDerivatives 4.0 International License. To view a copy of this license, visit <http://creativecommons.org/licenses/by-nc-nd/4.0/>

1 **NeuroImage special issue manuscript for: SI Spatio-temporal Limits**

2 **Techniques for blood volume fMRI with VASO: From low-resolution mapping towards sub-**  
3 **millimeter layer-dependent applications**

4 **Laurentius Huber<sup>a\*</sup>, Dimo Ivanov<sup>b</sup>, Daniel A. Handwerker<sup>a</sup>, Sean Marrett<sup>c</sup>, Maria Guidi<sup>d</sup>,**  
5 **Kâmil Uludağ<sup>b</sup>, Peter A. Bandettini<sup>a,c</sup>, and Benedikt A. Poser<sup>b</sup>**

6 <sup>a</sup> Section on Functional Imaging Methods, Laboratory of Brain and Cognition, NIMH, NIH,  
7 Bethesda, MD, USA

8 <sup>b</sup> Maastricht Brain Imaging Centre, Faculty of Psychology and Neuroscience, Maastricht  
9 University, Maastricht, The Netherlands

10 <sup>c</sup> FMRF, NIMH, NIH, Bethesda, MD, USA

11 <sup>d</sup> Max Planck Institute for Human Cognitive and Brain Sciences, Leipzig, Germany

12

13 \*Corresponding author:

14 Laurentius Huber, PhD

15 Section on Functional Imaging Methods, NIMH, National Institutes of Health

16 Building 10, Room 1D80B

17 10 Center Dr. MSC 1148

18 Bethesda, MD 20892-1148

19 Email: Laurentius.Huber@nih.gov

20 Phone: +1 301 402 7298

21

22 Running Title: Layer-dependent fMRI with VASO 3D-segmented-EPI

23

24 The body of the text contains 7483 words (with additional 3256 words in references)

25 **Highlights:**

- 26
- 27 • Limitations of sub-millimeter fMRI are discussed
  - 28 • CBV-sensitive fMRI is combined with 2D and 3D-segmented-EPI imaging
  - 29 • At ultra-high resolutions, novel contrast and acquisition schemes are needed
  - 30 • At high-res: 1.) CBV fMRI outperforms GE-BOLD 2.) 3D-segmented-EPI outperforms 2D-EPI
  - 31 • CBV fMRI based on 3D-segmented-EPI allow layer-dependent fMRI applications

32

33 **Abstract**

34 Quantitative cerebral blood volume (CBV) fMRI has the potential to overcome several  
35 specific limitations of BOLD fMRI. It provides direct physiological interpretability and  
36 promises superior localization specificity in applications of sub-millimeter resolution fMRI  
37 applications at ultra-high magnetic fields (7 T and higher). Non-invasive CBV fMRI using  
38 VASO (vascular space occupancy), however, is inherently limited with respect to its data  
39 acquisition efficiency, restricting its imaging coverage and achievable spatial and temporal  
40 resolution. This limitation may be reduced with recent advanced acceleration and

1 reconstruction strategies that allow two-dimensional acceleration, such as in simultaneous  
2 multi-slice (SMS) 2D-EPI or 3D-segmented-EPI in combination with CAIPIRINHA field-of-view  
3 shifting. In this study, we sought to determine the functional sensitivity and specificity of  
4 these readout strategies with VASO over a broad range of spatial resolutions; spanning from  
5 low spatial resolution (3 mm) whole-cortex to sub-millimeter (0.75 mm) slab of cortex (for  
6 cortical layer-dependent applications). In the thermal-noise-dominated regime of sub-  
7 millimeter resolutions, 3D-segmented-EPI-VASO provides higher temporal stability and  
8 sensitivity to detect changes in CBV compared to 2D-EPI-VASO. In this regime, 3D-  
9 segmented-EPI-VASO unveils task activation located in the cortical laminae with little  
10 contamination from surface veins, in contrast to the cortical surface weighting of GE-BOLD  
11 fMRI. In the physiological-noise-dominated regime of lower resolutions, however, 2D-SMS-  
12 VASO shows superior performance compared to 3D-segmented-EPI-VASO. Due to its  
13 superior sensitivity at a layer-dependent level, 3D-segmented-EPI VASO promises to play an  
14 important role in future neuroscientific applications of layer-dependent fMRI.

15 **Abbreviations:** BOLD = blood oxygenation level dependent; CAIPIRINHA (CAIPI) = Controlled  
16 Aliasing in Parallel Imaging Results in Higher Acceleration; CBV = cerebral blood volume;  
17 CNR = contrast-to-noise ratio; CSF = cerebrospinal fluid;  $\Delta$ CBV = change in CBV; EPI = echo  
18 planar imaging; fMRI = functional magnetic resonance imaging; FOV = field of view; GE =  
19 gradient echo; GM = grey matter; ROI = region of interest; SAR = specific absorption rate;  
20 SNR = signal-to-noise ratio; SS-SI VASO = slice-selective slab-inversion VASO; TE = echo time;  
21 TI = inversion time; TR = repetition time; VASO = vascular space occupancy.

22 **Keywords:** vascular space occupancy, SS-SI VASO, cerebral blood volume, simultaneous  
23 multi-slice, 3D-EPI, 7 Tesla MRI, layer-dependent fMRI.

## 24 1. Introduction

25 A detailed understanding of the organization of macroscopic brain areas into distinct  
26 networks requires a profound knowledge about the inter-area connections into  
27 functional building blocks of small cortical layers (Yacoub et al., 2015). The cortical grey  
28 matter (GM) ribbon consists of up to 6 of these histologically-defined cortical layers with  
29 thicknesses usually between 0.2 mm and 1 mm. Mapping the brain activity across thin  
30 cortical layers and their differential functional connectivity to distant brain areas would  
31 be highly valuable for human cognitive research. The only non-invasive *in vivo* imaging  
32 method currently capable of mapping brain activity at sub-millimeter resolutions, and  
33 hence having the potential ability to detect layer-dependent physiological signal  
34 changes, is functional magnetic resonance imaging (fMRI).

35 Conventional blood oxygenation level dependent (BOLD) fMRI methods, however, are  
36 most commonly applied at relatively coarse resolutions in the range of 2 - 4 mm. To  
37 increase the resolution to the sub-millimeter range (e.g. 0.75 mm), there are two major  
38 challenges that need to be addressed: First, the corresponding reduction in voxel  
39 volume of up to two orders of magnitude limits the available MRI signal-to-noise ratio

1 (SNR) and, thus, sensitivity to detect signal changes (contrast to noise ratio, CNR).  
2 Second, the BOLD-relevant oxygenation changes in draining veins (Menon et al., 1995;  
3 Turner, 2002) result in a reduced effective spatial resolution, independent of the  
4 nominal imaging resolution used. Engel et al. could quantify the spatial resolution in of  
5 fMRI at 1.5 T in retinotopy studies of the human visual cortex to be consistent with an  
6 area whose full width at half maximum (FWHM) spreads across 3.5 mm (Engel et al.,  
7 1997). At 3 T Parkes et al. could quantify the FWHM of conventional GE-BOLD and SE-  
8 BOLD with a rotating visual wedge paradigm to be 3.9 mm and 3.4 mm, respectively.  
9 Shmuel et al. investigated the regional specificity of BOLD fMRI at 7T in a flat (unfolded)  
10 region in V1. They found that, when the large veins are removed from the analysis, the  
11 FWHM of GE-BOLD is about 2 mm (1.52 mm shortly after stimulus onset and 2.42 mm 5  
12 seconds after stimulus onset).

13 It has been shown in animals e.g. (S.-G. Kim et al., 2013; Smirnakis et al., 2007) and in  
14 humans (Huber et al., 2015a) that fMRI contrasts based on cerebral blood volume (CBV)  
15 can map changes of brain activity with higher spatial specificity and without  
16 contamination of the remote draining veins compared to BOLD fMRI.

17 The most commonly used method for non-invasive measurements of CBV changes in  
18 humans is vascular space occupancy (VASO) (Lu et al., 2003). VASO takes advantage of  
19 the  $T_1$  difference between blood and surrounding tissue, and uses an inversion recovery  
20 pulse sequence to null blood signal while maintaining part of the tissue signal. The VASO  
21 signal intensity can thus be considered proportional to  $1 - \text{CBV}$ . When neural activation  
22 causes CBV to increase, the VASO signal will show a decrease, allowing the detection of  
23 activated regions in the brain (Lu and van Zijl, 2012). VASO is particularly attractive at  
24 high fields (7 T) due to the increase in image SNR and the longer longitudinal relaxation  
25 time of blood, which can amplify VASO's functional  $T_1$ -contrast (Huber et al., 2014b).  
26 However, as the VASO contrast relies on elimination of the intravascular signal, it  
27 requires image acquisition after an inversion pulse has been applied at the blood  
28 magnetization nulling time. Dependent on the VASO variant used, the blood nulling  
29 time does not only depend on blood's  $T_1$ , but also on the dynamic steady-state of the  
30 sequence including the respective flipangles and TRs. Independent of the VASO variant  
31 used, there is only a short acquisition window of blood nulling to acquire the signal.  
32 Hence, if multiple consecutive slices are acquired after each inversion, they end up with  
33 different inversion times ( $T_i$ ), allowing only a small number of slices to be acquired,  
34 which limits the achievable brain coverage of VASO using standard EPI readout. To  
35 increase the imaging coverage without unacceptable penalties in image quality, VASO  
36 has been combined with other readout strategies at 3 T, for instance, 3D-GRASE,  
37 TFL/FFE, and 3D-HASTE (Cheng et al., 2014b; Lu et al., 2004; Poser and Norris, 2011,  
38 2009).

1 Significant gains in both spatial resolution and spatial coverage at ultra-high field  
2 without compromising SNR losses may be achieved by incorporating recent  
3 improvements in accelerated acquisition techniques. In terms of sampling efficiency, the  
4 most important innovation since the introduction of EPI itself is EPI with simultaneous  
5 multi-slice imaging (SMS). SMS uses multi-band (MB) excitations to simultaneously  
6 excite multiple slices and use the coil sensitivity profiles to disentangle the signals from  
7 the different slices (Feinberg and Setsompop, 2013; Feinberg et al., 2010; Larkman et al.,  
8 2001; Moeller et al., 2010). As a result, the volume acquisition time is reduced by the  
9 nominal slice acceleration factor. Together with blipped-CAIPIRIHA sampling, SMS-EPI  
10 has been shown to achieve high slice and in-plane acceleration factors with minimal g-  
11 factor penalty (a measure of SNR loss in accelerated acquisition schemes (Setsompop et  
12 al., 2012)). SMS-EPI was rapidly adopted in all MRI modalities based on 2D-EPI readout,  
13 including BOLD (Feinberg et al., 2010), diffusion (Setsompop et al., 2012), CBF (Feinberg  
14 et al., 2013; Ivanov et al., 2016a; T. Kim et al., 2013) and CBV imaging (Huber et al.,  
15 2016a).

16 An alternative to sequential 2D multi-slice imaging is volumetric 3D-segmented-EPI  
17 (Poser et al., 2010) acquisition, which allows equivalent acquisition speedup and can  
18 also be combined with CAIPIRINHA sampling (Narsude et al., 2016; Poser et al., 2013) to  
19 yield g-factor benefits that are analogous to SMS-EPI (Zahneisen et al., 2015, 2014).

20 Earlier work at 3 and 7 T has investigated the relative merits of 2D and 3D acquisitions  
21 for BOLD fMRI (Lutti et al., 2013; Stirnberg et al., 2016), but neither did so systematically  
22 at different spatial resolutions nor below 1 mm<sup>3</sup>. For high resolution, low image SNR  
23 acquisitions, the inherent SNR advantage of volumetric acquisition may become an  
24 important contribution in pushing the spatial boundaries of fMRI applications. This SNR  
25 advantage is coming from the fact that volumetric slab-excitation allows the whole  
26 magnetization to be acquired several times in a time scale that is approaching the  
27 relaxation times.

28 In this paper, we discuss and investigate the limitations and the applicability of CBV fMRI  
29 from resolutions of 3 mm to 0.75 mm (layer-dependent). Specifically, we focus on the  
30 relative amounts of thermal and physiological noise, and signal stability with decreasing  
31 voxel sizes, and local specificity to cortical layers.

32 Aiming towards layer-dependent neuroscience applications, we compare gradient echo  
33 (GE) BOLD and CBV-VASO contrast mechanisms and 2D-SMS and 3D-segmented-EPI  
34 readout strategies across a wide range of resolutions. We elaborate on the limitations  
35 and challenges specific to sub-millimeter layer-dependent fMRI and show how new  
36 approaches, such as 3D-segmented-EPI VASO, hold promise to cope with them.

## 37 **2. Materials and Methods**

### 38 **2.1. MR sequence and setup**

1 Ten healthy right-handed volunteers (age 22-42 years) participated after granting  
2 informed consent under an NIH Combined Neuroscience Institutional Review Board-  
3 approved protocol (93-M-0170) in accordance with the Belmont Report and US  
4 Federal Regulations that protect human subjects. Slice-selective slab-inversion (SS-SI)  
5 VASO (Huber et al., 2014b) with 2D-SMS and 3D-segmented-EPI readout was  
6 implemented on a MAGNETOM 7 T scanner (Siemens Healthcare, Erlangen, Germany)  
7 using the vendor provided IDEA environment (VB17A-UHF). For RF transmission and  
8 reception, a single-channel-transmit/32-channel receive head coil (Nova Medical,  
9 Wilmington, MA, USA) was used. The scanner was equipped with a SC72 body  
10 gradient coil (maximum effective gradient strength used here: 49 mT/m; maximum  
11 slew rate used: 199 T/m/s). The timing of magnetization preparation and interleaved  
12 acquisition of VASO and BOLD data is schematically depicted in Fig. 1 **(A)-(C)**. The  
13 timing of the acquisitions is:  $T_1/T_2/TR = 1100/2600/3000$  ms across all experiments.  
14 The blood-nulling time is calculated based on the assumed value of blood  $T_1 = 2100$  ms  
15 (Grgac et al., 2012; Hales et al., 2015), following earlier VASO studies at 7 T (Huber et  
16 al., 2016a, 2014a). The adiabatic VASO inversion pulse is based on the TR-FOCI pulse  
17 (Hurley et al., 2010) (Fig. 1 **(A)-(B)**). The pulse duration was 10 ms and the bandwidth  
18 was 6.3 kHz. For sequence parameters regarding the signal acquisition (excitation,  
19 acceleration, resolution), see the section below.

20 VASO can be contaminated by inflow of non-inverted blood, especially when blood  $T_1$   
21 is not much shorter than the TR (Donahue et al., 2009). These inflow effects can be  
22 minimized, when the blood-nulling time is shorter than the time that blood needs to  
23 arrive from the arteries in the neck to the micro vessels of the imaging slice (Huber et  
24 al., 2016a). Here, a  $T_1 = 1100$  ms was chosen, which includes an additional leeway of  
25 200 ms compared to the estimated arterial arrival time in the sensorimotor cortex  
26 (Mildner et al., 2014). The blood-nulling time was manipulated by means of an  
27 adjusted inversion efficiency of 87% in a  $B_1$ -independent manner by using a phase skip  
28 (Fig. 1 **(A)-(B)**) of the RF field during inversion as described in (Huber et al., 2014b).  
29 The inversion pulse amplitude was adjusted to have a minimum of 10  $\mu$ T down to the  
30 Circle of Willis across all participants by using a transmitter voltage of 320 V (max  
31 during TR-FOCI pulse).

32 With increasing field strength, the positive BOLD signal change during neural  
33 activation increasingly counteracts the negative VASO signal change (Lu and van Zijl,  
34 2005). The GE-BOLD effect typically has two components: intravascular and  
35 extravascular. At 7 T, the extravascular BOLD signal dominates the intravascular BOLD  
36 signal by more than 90% (Donahue et al., 2010; Uludag et al., 2009). This extravascular  
37 BOLD contamination is considerably larger than the desired VASO signal change and  
38 needs to be corrected for to obtain quantitative CBV. In SS-SI VASO, an interleaved,  
39 pair-wise acquisition (Fig. 1 **(A)-(B)**) of VASO and BOLD images is used to distinguish  
40 between BOLD and VASO signal components of the resulting signal. When the pure

1 BOLD contrast contribution is known, the BOLD contamination in the VASO image can  
2 be factored out, as described earlier (Huber et al., 2014b).

3 In order to show the specific challenges of layer-dependent fMRI applications  
4 compared to the ones performed at conventional voxel sizes, experiments were  
5 conducted at 3 mm, 1.5 mm and 0.75 mm resolutions, for both 3D-segmented-EPI and  
6 2D-SMS-EPI. Seven participants were scanned at each resolution. To obtain best  
7 results at the respective resolutions, the FOV, the slice position, and acceleration  
8 factors were optimized individually for the 3 mm, 1.5 mm and 0.75 mm protocols, but  
9 kept identical for the 2D-SMS VASO and 3D-segmented-EPI acquisitions at each  
10 resolution.

11 These resolution-dependent acquisition parameters are listed as follows:

12

### 2.1.1. 3 mm setup: low-resolution whole-cortex coverage case

Whole-cortex coverage was achieved with the following acquisition parameters: 33 tilted axial slices, nominal slice thickness 3 mm, nominal in-plane resolution  $3.0 \times 3.0 \text{ mm}^2$ , TE = 12 ms, partial Fourier = 6/8, in-plane GRAPPA 3, through-plane acceleration 3, CAIPI FOV-shift = 1/2 (was chosen based on the performance in pilot experiments), in-plane phase-encoding direction: anterior-posterior.

### 2.1.2. 1.5 mm setup: GM-specific application case

24 tilted axial slices were positioned to cover the sensorimotor regions of both hemispheres with: TE = 17 ms, nominal slice thickness 1.5 mm, nominal in-plane resolution  $1.5 \times 1.5 \text{ mm}^2$ , partial Fourier = 6/8, in-plane GRAPPA 2, through-plane acceleration 2, CAIPI FOV-shift = 1/3, in-plane phase-encoding direction: anterior-posterior.

### 2.1.3. 0.75 mm setup: layer-dependent application case

10 tilted axial slices were positioned to cover the left motor cortex. Slices were rotated until the major region of the thumb representation (next to index finger) was imaged in slices perpendicular to the cortical surface with: TE = 24 ms, nominal slice thickness 1.5 mm, nominal in-plane resolution  $0.75 \times 0.75 \text{ mm}^2$ , in-plane GRAPPA 2, asymmetric matrix size  $32 \times 96$ , in-plane phase-encoding direction left-right. No through-plane acceleration or CAIPI FOV-shifting was applied for this protocol. To minimize  $T_2^*$ -blurring, partial Fourier imaging was kept as conservative as possible at 7/8 (Huber et al., 2015c).

### 2.1.4. Direct comparison across resolutions

Optimal acceleration parameters are highly dependent on the desired resolution, volume coverage and time constraints (TI/TR). For example, larger FOVs with more slices allow higher acceleration factors than smaller FOVs with only few slices, where the spatial encoding by the coil-array is limited. Moreover, larger voxels allow shorter EPI echo-spacing. Hence, the acquisition/acceleration parameters of the different setups investigated above were optimized differently for the respective resolutions chosen. For a more direct comparison of 2D-SMS and 3D-segmented-EPI readouts, we conducted additional tSNR experiments with identical acceleration parameters and in-plane resolutions, but varying slice thicknesses in 3 participants. Scan parameters were as follows: Matrix:  $64 \times 64$ , 8 slices, nominal in-plane resolution  $1.0 \times 1.0 \text{ mm}^2$ , no through-plane GRAPPA, in-plane GRAPPA 2, TE = 24 ms. The slice thickness varied between 0.3 mm and 10 mm.



### 1           **2.1.5. Investigation of the effect of head motion**

2           In order to investigate the effect of task-correlated head motion in 3D-  
3           segmented-EPI and 2D-SMS VASO, we utilized data from 8 experiments in N = 4  
4           participants during a Valsalva breathholding task, which can have a large task-  
5           correlated head motion. For imaging, the 1.5 mm protocol was used as  
6           described above.

### 7           **2.2. In-plane acceleration parameters**

8           The acquisition order of the GRAPPA reference lines followed the FLEET approach  
9           shown for 2D EPI (Polimeni et al., 2016), and its analogue for 3D-segmented-EPI  
10          acquisitions (Ivanov et al., 2015). That is, in-plane segmented reference line  
11          acquisition is ordered such that all in-plane (line) segments for a given slice (2D EPI) or  
12           $k_z$ -encoding step (3D-segmented-EPI) are acquired in immediate succession before  
13          proceeding to the next slice or  $k_z$ -encode step. This minimizes segmentation artifacts  
14          and results in superior conditioning of the subsequent GRAPPA reconstruction and  
15          correspondingly increased tSNR. The vendor's GRAPPA (Griswold et al., 2006)  
16          reconstruction algorithms were applied using a  $3 \times 4$  (read direction x phase direction)  
17          kernel. Partial Fourier reconstruction (Jesmanowicz et al., 1998) was done with the  
18          projection onto convex sets (POCS) algorithm (Haacke et al., 1991) with 8 iterations.  
19          Finally, the complex coil images were combined using the vendor's implementation of  
20          sum-of-squares.

### 21          **2.3. 2D-SMS specific parameters**

22          The nominal slice-selective excitation pulse flip angle was  $70^\circ$  with a pulse duration of  
23          2.5 ms. The summation of multi-band sinc-pulses was conducted with optimized phase  
24          schedules for minimizing peak RF power (Wong, 2012) (see corresponding pulse shape  
25          in Fig. 1 (D)). Online reconstruction on the scanner was performed using a  
26          combination of the vendor software and the SMS reconstruction as distributed with  
27          the MGH blipped-CAIPI C2P (<http://www.nmr.mgh.harvard.edu/software/c2p/sms>).  
28          SMS signals were first un-aliased with an implementation of SplitSlice-GRAPPA with  
29          LeakBlock (Cauley et al., 2014) and a  $3 \times 3$  SliceGRAPPA kernel before entering in-  
30          plane reconstruction as described above.

### 31          **2.4. 3D-segmented-EPI specific parameters:**

32          The 3D VASO sequence was based on a previous 3D-segmented-EPI implementation  
33          (Poser et al., 2010) with support for CAIPIRINHA sampling (Poser et al., 2013). Online  
34          reconstruction was performed using a combination of standard scanner software and  
35          a vendor-provided works-in-progress implementation of GRAPPA CAIPIRINHA  
36          (Siemens software identifier: IcePAT WIP 571) with kernel size  $4 \times 3 \times 3$ .

1 For direct comparability with the 2D-SMS acquisitions, we used the same in-plane  
2 readout (for identical distortions and  $T_2^*$ -blurring) and no slab-oversampling (for same  
3 number of imaging shots per inversion). 3D slice aliasing was minimized using a sharp  
4 slab-excitation pulse profile with a bandwidth-time-product of 25.

5 The need for magnetization inversion and the need for long volume TR in VASO results  
6 in 3D-segmented-EPI segments being acquired in a non-steady state. Hence, in order  
7 to minimize any  $T_1$ -related blurring along the slice direction (Gai et al., 2011),  
8 individual excitation pulse flip angles were varied along the train of  $k_z$ -planes to ensure  
9 similar signal for every shot. The last excitation pulse of every readout was chosen to  
10 be nominally  $90^\circ$ . To keep the same signal across  $k$ -space segments, the flip angles of  
11 the preceding segments were adjusted to be respectively smaller. Depending on the  
12 number of segments, the first excitation pulse flip angle desired to be between  $16^\circ$ -  
13  $22^\circ$ . For instance, the 0.75 mm protocol, the nominal flip angles adjusted in the  
14 sequence code to be:  $21.8^\circ$ ,  $22.5^\circ$ ,  $23.4^\circ$ ,  $24.3^\circ$ ,  $25.5^\circ$ ,  $26.8^\circ$ ,  $28.4^\circ$ ,  $30.5^\circ$ ,  $33.3^\circ$ ,  $37.3^\circ$ ,  
15  $43.7^\circ$ ,  $57.4^\circ$ ,  $90.0^\circ$ ). The  $T_1$ -relaxation between consecutive excitation pulses was  
16 estimated assuming a tissue  $T_1$ -value of 1800 ms at 7 T (Wright et al., 2008).

17 To be most comparable with the 2D-SMS acquisition scheme and obtain identical  
18 distortions and  $T_2^*$ -blurring, the number of slices in 2D-SMS and the number of  
19 segments in 3D-segmented-EPI were kept the same. Thus, in every 3D-segmented-EPI  
20 shot, one whole slice of  $k$ -space was acquired.

## 21 **2.5. SAR values**

22 The overall energy deposition of the sequence never exceeded 2.1 W/kg, according to  
23 the SAR estimation of the vendor. Due to the considerable SAR contribution from the  
24 inversion pulse and the high bandwidth-time-product of 25 in 3D-segmented-EPI, the  
25 estimated SAR values for 3D-segmented-EPI were not much lower than for the 2D-  
26 SMS EPI. The values were 1.9/2.1 W/kg (3D-segmented-EPI/2D-SMS EPI) for the high  
27 resolution (0.75 mm) and 1.3/2.1 W/kg for the low resolution (3 mm) protocol.

## 28 **2.6. fMRI task**

29 The sensitivity of each protocol to functional activation was investigated with a  
30 unilateral finger tapping tasks: one-minute blocks (30 s rest and 30 s, paced tapping  
31 with 0.75 Hz) repeated 12 times. This resulted in 12-minute acquisitions for each  
32 protocol, plus 20 s – 40 s before and after the 12 blocks, respectively.

33 The effect of task-correlated head motion was investigated with a Valsalva  
34 breathholding task. This task consists of breathholding with additional chest pressure  
35 increase (Wu et al., 2015). This task has the potential for efficient high CNR mapping of  
36 vascular reactivity. However, its application with VASO is often limited with unwanted  
37 motion artefacts arising from correlated head tilting, which made it an ideal control

1 for examining head motion. Each run consisted of 10 breathholding periods of 15 s  
2 interspaced with 45 s of paced breathing.

### 3 **2.7. Data analysis**

4 All MR images were motioncorrected using SPM8 (Functional Imaging Laboratory,  
5 University College London, UK). The outermost slices were excluded from the analysis  
6 to minimize motion artifacts and residual 3D-segmented-EPI related slab fold-over  
7 artifacts. Activation GLM analysis was done using FSL FEAT (Version 5.98) (Worsley,  
8 2001) with a cluster threshold of 10 voxels (applied with AFNI (Cox, 1996)). No signal  
9 smoothing was applied at any point during the analysis to minimize losses of spatial  
10 specificity (Stelzer et al., 2014).

11 The tSNR was separately estimated for BOLD and VASO timeseries after respective  
12 signal detrending with AFNI (Cox, 1996). The tSNR was computed over 480 time steps  
13 (240 for VASO and 240 for BOLD).

14 The VASO SNR was estimated by the method described for time series imaging  
15 (Feinberg et al., 2013; Glover and Lai, 1998): The even- and odd-numbered time points  
16 of VASO were separately averaged, and the sum and difference of these two images  
17 were calculated. Note, that the even- and odd-numbered time points refer to the  
18 same VASO contrast. They do not refer to the interleaved acquisition of VASO and  
19 BOLD in the MR sequence. The VASO SNR was calculated as the mean value across M1  
20 ROIs in the sum image divided by the standard deviation across the same region in the  
21 difference image. BOLD SNR was calculated analogously by taking the even- and odd-  
22 numbered time points of the BOLD time series.

### 23 **2.8. Layer-analysis**

24 The analysis to plot functional signal changes across cortical depth followed the  
25 description in (Huber et al., 2015b). In short: GM-CSF borders and GM-WM borders for  
26 the primary motor cortex “hand knob” were manually drawn on the EPI images.  
27 Cortical depths were calculated based on the equi-volume principle (Waehnert et al.,  
28 2014). No significance thresholding was applied to avoid biases of variable detection  
29 thresholds across cortical depth (Goense et al., 2012a).

## 30 **3. Results**

### 31 **3.1. tSNR across resolutions with optimized parameters**

32 Results of the tSNR across resolutions are shown in Fig. 2 for one representative  
33 participant. 2D-SMS VASO has higher tSNR values compared to 3D-segmented-EPI at  
34 conventional resolutions of 1.5 mm and 3 mm. In the thermal-noise-dominated  
35 regime of sub-millimeter resolutions (0.75 mm), this relationship becomes inverted  
36 and 3D-segmented-EPI outperforms the 2D-SMS VASO in terms of tSNR. The mean

1 tSNR values shown in Fig. 2 refer to values averaged over M1 ROIs across participants  
2 (N = 7 in Fig. 2 **(A)-(B)**). With the individually optimized acquisition parameters  
3 (acceleration factor and FOV) across protocols, tSNR of GM is above 20 throughout all  
4 resolutions shown in Fig. 2 **(A)-(B)**. This means that the strong response of a finger  
5 tapping task should exceed the detection threshold with a 12 min fMRI experiment  
6 (Murphy et al., 2007).

7 To reveal the tSNR sensitivity across resolutions independent of GRAPPA and  
8 bandwidth effects, the signal stability for the same imaging readout (1mm<sup>2</sup> in-plane  
9 resolution) is depicted for different slice thicknesses in Fig. 2 **(C)**. tSNR values refer to  
10 the average across all 3 participants acquired with this protocol. The curves for 2D-  
11 SMS and 3D-segmented-EPI VASO show an asymptotic behavior that is qualitatively  
12 very similar to the ones shown in previous studies that have investigated the tSNR-  
13 SNR relationship across resolutions (Murphy et al., 2007; Triantafyllou et al., 2011). To  
14 stress that the tSNR saturation is arising from physiological noise contributions, image  
15 SNR is depicted in Fig. 2 **(D)**. Image SNR does not show the strong saturation at larger  
16 voxel volumes and 3D-segmented-EPI has higher values compared to 2D-SMS for each  
17 resolution. Fig. 2 **(E)-(H)**, depict that same quantities as in Fig. 2 **(A)-(D)** but for the  
18 BOLD signal. Please note the different scaling of colorbars and y-axes.

19 The consistency of these results across participants can be seen in Fig. 3.

### 21 **3.2. Sensitivity to detect functional activation**

22 Functional activation maps for the unilateral finger-tapping task are shown in Fig. 4 for  
23 one representative subject. The depicted MRI slices are the same as shown in Fig. 2  
24 **(A)-(B)**. Simultaneously acquired functional maps of BOLD signal change are included  
25 in order to stress the different spatial patterns of BOLD fMRI compared to CBV-fMRI.  
26 Note that the quantitative VASO contrast is inverted to obtain estimates of blood  
27 volume in units of ml per 100 ml of tissue (Huber et al., 2015a).

28 For the low resolution of 3 mm, 2D-SMS and 3D-segmented-EPI activation maps show  
29 M1 activation in a very similar fashion (Fig. 4 **(E), (K)**). Note that this is the case despite  
30 the  $\approx$  50% higher tSNR in 2D-SMS compared to 3D-segmented-EPI. This is most likely  
31 due to the fact that both readout strategies are well above the detection threshold for  
32 a finger-tapping task.

33 At 1.5 mm resolutions, the voxel size approaches the distance between the  
34 neighboring GM ribbons of the central sulcus. Hence, the intracortical CBV signal  
35 changes of M1 and S1 start to separate into two distinct clusters of voxels (blue  
36 arrows in Fig. 4 **(C), (I)**). Due to the presence of large draining veins above the cortical

1 surface, functional activation in GE-BOLD fMRI, on the other hand, appears as one big  
2 cluster (blue arrows in Fig. 4 **(J)**).

3 For layer-dependent fMRI applications of 0.75 mm resolutions, both 2D-SMS VASO  
4 (Fig. 4 **(A)**) and 3D-segmented-EPI VASO (Fig. 4 **(G)**) have enough sensitivity to detect  
5 tapping-induced activity in M1. Due to the higher SNR in 3D-segmented-EPI VASO  
6 layer-dependent activity features are slightly more obvious (green arrow in Fig. 4 **(G)**)  
7 compared to the 2D-SMS VASO (Fig. 4 **(A)**). Even though, there might be some layer-  
8 dependent features visible in GE-BOLD data (Fig. 4 **(B), (H)**), most of the signal change  
9 appears to be dominated from nonspecific superficial veins.

10 Please, note the different scaling of the functional responses across resolutions and  
11 correspondingly different colorbars in Fig. 4. This was done to account for the larger  
12 signal changes at high resolutions when partial volume effects are minimized.

### 13 **3.3. Susceptibility to task-correlated head motion**

14 During Valsalva breathholding tasks, participants showed considerable head motion.  
15 Particularly pitch rotation turned out to be highly correlated with the breathholding  
16 task. A motion trace of SPM motion estimation is shown in Fig. 5 **(A)** for one  
17 representative subject. Such motion can result in considerable motion artefacts during  
18 fMRI response evaluation. Fig. 5 **(B)-(C)** show sagittal views of averaged VASO signal  
19 intensities across slices. It can be seen in 2D-SMS-VASO that very small deviations of  
20 the effective inversion time results in corresponding inhomogeneities in  $T_1$ -weighting  
21 and signal intensity across slices. This means that any retrospective motion correction  
22 will interpolate these signal inhomogeneities across slices. In 3D-segmented-EPI VASO  
23 on the other hand, all slices have the same effective inversion time and retrospective  
24 motion correction can be applied without the introduction of motion artefacts.

### 25 **3.4. Bias of baseline vasculature:**

26 The sole fact that specific signal variations across cortical depth can be observed, does  
27 not prove layer-specificity, when the underlying physiology is unknown. This is  
28 established in the field and has been discussed already in the literature (Koopmans et  
29 al., 2011, 2010). According to these discussions, the depth-dependent variations in  
30 fMRI signal could simply resemble the baseline vascular distribution. Following  
31 suggestions in (Goense et al., 2016), we tried to minimize incorrect interpretations  
32 due to this bias by applying multi-modal fMRI and directly comparing it to estimates of  
33 the baseline vasculature as done in Fig. 6 **(G)-(H)**. Since the functional profiles in Fig. 6  
34 **(C)-(D)** are qualitatively different from Fig. 6 **(G)-(H)**, the peak fMRI responses can be  
35 considered to be caused by task-specific layer-dependent activation, and not by the  
36 baseline vasculature distribution.

## 37 **4. Discussion**

1 The results shown in Figs. 2-3 demonstrate the advantages and disadvantages of VASO and  
2 BOLD fMRI with 2D-SMS and 3D-segmented-EPI acquisitions across a broad range of  
3 resolutions. The results can be taken as evidence that in the case of layer-dependent  
4 applications, the conventional contrast mechanisms and readout strategies that perform  
5 very well at 2 – 4 mm spatial resolutions may no longer be the most suitable choice. Instead,  
6 less utilized readout strategies, like 3D-segmented-EPI, and fMRI contrasts, like VASO, might  
7 provide superior tools for neuroscientific applications that require spatial specificities in the  
8 sub-millimeter regime.

#### 9 **4.1. Benefits of 3D-segmented-EPI at high resolutions**

10 3D-EPI acquisition approaches were originally suggested in (Mansfield et al., 1995;  
11 Song et al., 1994). In recent years they have gained considerable interest (Gai et al.,  
12 2011; Jorge et al., 2013; Langkammer et al., 2015; Lutti et al., 2013; Van Der Zwaag et  
13 al., 2012) due to the flexibility of having an additional  $k$ -space dimension. For instance,  
14 3D acquisition strategies allow partial Fourier imaging along the  $k_z$  direction to provide  
15 reduction in volume TR (Poser et al., 2010). Furthermore, 3D acquisitions allow thin  
16 slices without being limited by excitation pulse imperfections (Poser et al., 2010). They  
17 are less prone to motion-induced spin-history effects than 2D imaging since the whole  
18 slab or volume is always excited, and - importantly - they allow undersampling to be  
19 applied along both the in-plane and through-plane phase-encoding directions  
20 (Narsude et al., 2016; Poser et al., 2014, 2010). With the incorporations of controlled  
21 aliasing,  $g$ -factors can be reduced to a minimum (Narsude et al., 2016; Poser et al.,  
22 2013), allowing high total acceleration factors and correspondingly fast temporal  
23 sampling. Due to the smaller excitation flip angles used in 3D-segmented-EPI  
24 compared to 2D-SMS EPI, 3D-segmented-EPI applications have been suggested to be  
25 beneficial at high field strengths, where SAR constraints can limit the number of slices  
26 and the TR (Gai et al., 2011; Poser et al., 2010).

27 One likely reason, why 3D-segmented-EPI has not become as widely applied as single  
28 shot 2D-SMS EPI, however, comes from the fact that it is more sensitive to  
29 physiological noise components: while the very fast acquisition of 2D-SMS-EPI in the  
30 range of few tens of ms ‘freezes out’ cardiac- and respiration-induced signal  
31 fluctuations, the extended sampling window in 3D-segmented-EPI, of the order of few  
32 hundreds of ms, approaches the timescale of physiological variations. These  
33 physiological modulations across the  $k$ -space acquisition can result in increased signal  
34 fluctuations all across the entire image space and limit the fMRI sensitivity

35 In addition to the different physiological noise contributions, that need to be dealt with  
36 differently in 3D-EPI (Jorge et al., 2013; Lutti et al., 2013), 2D-EPI and 3D-EPI have different  
37 sequence timing requirements due to 3D-EPI relaxation time differences across slices.  
38 Inversion recovery 3D-EPI methods that segment volume  $k$ -space across TRs (van der  
39 Zwaag et al., 2016), can account for this to allow the same flexibility as a 2D readout.

1        However, pulse sequences using these methods are not widely distributed across MRI scanner  
2        vendors..

3        The results of the study presented here confirm this notion and provide evidence that  
4        in the physiological-noise-dominated regime of conventional voxel sizes of 1.5 – 3 mm,  
5        2D-SMS VASO provides higher signal stability compared to 3D-segmented-EPI VASO  
6        (Fig. 1 **(A)-(B)**). At ultra-high resolutions, however, in the thermal-noise-dominated  
7        regime, the advantage of increased image SNR becomes more important and 3D-  
8        segmented-EPI acquisitions become more stable than 2D-SMS approaches (Fig 1 **(C)**).

#### 9        **4.2. 3D-segmented-EPI in inversion recovery sequences**

10        In inversion-recovery sequences such as for VASO or ASL applications,  $T_1$ -relaxation  
11        processes can affect the image contrast while a volume is being acquired. In 2D-SMS  
12        sequences, the individual slice-groups are acquired consecutively. This means that  
13        adjacent slices can have different  $T_1$ -weightings. For short TIs ( $<$  tissue  $T_1$ ), this can  
14        result in different signal intensity across the brain volume imaged (blue arrows in Fig.  
15        1 **(A)**), with resulting inhomogeneous tSNR across the brain (blue arrows in Fig. 2  
16        **(A)**). The fact that in 3D-segmented-EPI the entire brain volume has the same  
17        effective TI can be advantageous to quantify blood volume in VASO (Cheng et al.,  
18        2014a; Hua et al., 2013), to quantify  $T_1$  (Huber et al., 2016b; Marques et al., 2010), or  
19        to quantify CBF across slices (Gai et al., 2011; Ivanov et al., 2016b). When the  
20        effective inversion time is constant across slices, the functional contrast (e.g. blood  
21        nulling) is less biased by incomplete blood nulling, which could hamper CBV  
22        quantification in VASO experiments (Glielmi et al., 2009).

23        The different effective  $T_1$ -weighting and the correspondingly different signal across  
24        k-space segments in 3D-segmented-EPI, however, can result in inhomogeneous  
25        signal distribution across k-space accompanied by image blurring along the second  
26        phase encoding direction. To account for this and preserve the available MR signal  
27        across k-space segments, a flip angle modulation was used here following previous  
28        studies (Gai et al., 2011).

29        It must be noted, however, that this approach of using variable flip angles can only  
30        serve as a first order correction to minimize  $T_1$ -related blurring in the second phase-  
31        encoding (segment) direction. There are numerous higher-order effects that can not  
32        be corrected for with this approach. For instance, the approach of variable flip angles  
33        can be optimized for one  $T_1$ -compartment, only. Here, the nominal flip angles are  
34        adjusted to the  $T_1$  of GM. This means that the blurring effect in WM and CSF are only  
35        partly accounted for. Hence the point-spread-function is expected to be different  
36        across different tissue types comparable to conventional so-called anatomical  
37        sequences like MPRAGE or MP2RAGE. Furthermore, the approach of variable flip  
38        angles is limited by the inhomogeneities in RF transmit field at 7T. Hence, in brain

1 regions with particularly high or low  $B_1^+$  field strengths, the  $T_1$ -related blurring effect  
2 might be only partially accounted for.

### 3 **4.3. Benefits of VASO compared to GE-BOLD at lower resolutions**

4 The main benefits of VASO compared to BOLD are its quantifiability (Lu et al., 2003)  
5 and local specificity (Jin and Kim, 2006).

6 The 3 mm protocol used in this study is optimized to obtain fast whole cortex  
7 coverage. At these resolutions, it is not expected that CVB-fMRI offers a higher  
8 specificity than GE-BOLD (Turner, 2002). However, it might still be beneficial to apply  
9 VASO with this protocol, e.g. in studies, when its quantitative nature becomes  
10 important (Guidi et al., 2016; Kazan et al., 2015).

11 The results from the 1.5 mm protocol used in this study show the higher localization  
12 specificity to GM of VASO compared to GE-BOLD signal (blue arrows in Fig. 4 **(I)-(J)**).  
13 This is consistent with earlier studies (Huber et al., 2016a) and might be advantageous  
14 to separate close brain areas (e.g. M1 and S1) in network analysis or to minimize  
15 cancellation of positive and negative fMRI responses in neighboring regions (Huber et  
16 al., 2016a).

17 A disadvantage of VASO compared to GE-BOLD is its reduced sensitivity with fewer  
18 activated voxels detected (see voxel cluster size in Fig. 4 **(C)-(D)** and **(I)-(J)**). VASO is  
19 furthermore limited by its reduced imaging efficiency, resulting from the acquisition  
20 delay that is required for  $T_1$ -contrast to develop. Hence, to obtain an artifact-free  
21 VASO contrast, TR cannot be reduced to significantly below 3 s. The efficiency of BOLD  
22 fMRI, in contrast, is only limited by acquisition speed without comparable dead times  
23 as in VASO fMRI.

24 Considering the different imaging efficiency of the two fMRI methods, sensitivity  
25 comparisons between VASO and BOLD contrasts must be interpreted with caution.  
26 Here, we can only compare VASO experiments at its optimal TR of 3 s compared to  
27 BOLD experiments at the same TR of 3 s. But with the data acquired in this study, we  
28 cannot compare optimal VASO experiments with optimal BOLD experiments having  
29 shorter TRs of 1 s. For higher temporal resolution in BOLD fMRI, physiological noise  
30 can be sampled below the Nyquist rate, which can help to improve the functional  
31 sensitivity of BOLD fMRI even further (Stirnberg et al., 2016).

### 32 **4.4. Effect of head motion**

33 We investigated the effect of head motion during a Valsalva breathholding tasks with  
34 2D-SMS-VASO and 3D-segmented-EPI VASO. We find that having the same effective  
35 inversion times across slices in 3D-segmented-EPI-VASO makes it more suitable for  
36 retrospective motion correction compared to 2D-SMS-EPI. Results shown in Fig. 5



1 suggest that even at resolutions of 1.5 mm, where 2D-SMS-VASO provides higher  
2 sensitivity than 3D-segmented-EPI-VASO, one might want to refrain from 2D-SMS-  
3 VASO applications. It must be noted that the motion artefacts shown in Fig. 5 are most  
4 probably referring to head tilting between TRs of the sequence. The artefacts are likely  
5 not caused from head tilting during the relatively short acquisition windows. Hence,  
6 the apparent motion can be appropriately corrected retrospectively using rigid-body  
7 transformations. Motion during the acquisition window itself, however, can result in  
8 different artefacts that are harder to correct for (Ladstein et al., 2016). While the 3D-  
9 segmented-EPI can better account for contrast inhomogenies across slices compared  
10 to 2D-SMS-EPI, this does not mean that it can account better for other shortcomings  
11 when head motion is present. For instance, inter-TR and intra-TR head motion will also  
12 have a smoothing effect in 3D-EPI, while in the 2D EPI there would be fluctuations due  
13 to spin history effects.

#### 14 **4.5. Functional specificity**

15 The high-resolution results given in Figs. 3 **(A)**, **(C)**, **(G)**, **(I)** show that VASO fMRI can  
16 better delineate individual GM territories compared to GE-BOLD, which shows largest  
17 activation between the opposing GM banks of a sulcus. In addition, the specificity  
18 within cortical layers and the activity pattern following the cortical ribbon; Fig. 4 **(G)**  
19 suggest high localization specificity of CBV-fMRI compared to GE-BOLD signal. This is  
20 consistent with previous comparisons of CBV-fMRI and BOLD fMRI (Goense et al.,  
21 2007; Huber et al., 2015b; Kim and Ogawa, 2012) and one of the original motivations  
22 to do CBV-based fMRI.

#### 23 **4.6. Layer-dependent responses in light of the underlying physiology**

24 For conventional 3 mm voxels, CBF, CBV, and BOLD usually co-vary and are related to  
25 oxygen metabolism. With layer-dependent sub-millimeter voxels, however, observed  
26 neuro-vascular coupling may be altered (Goense et al., 2012a) and a combined  
27 acquisition of BOLD with CBF/CBV-based fMRI methods are required (Huber et al.,  
28 2016a) to provide additional information about neurovascular coupling, and to aid  
29 modeling and interpretation of high-resolution fMRI (Goense et al., 2016).

30 As indicated in Fig. 6 **(E)-(H)**, at layer-dependent resolutions, vascular and neuronal  
31 heterogeneities of the cortex, approach the scale of functional resolutions. Hence, to  
32 accurately predict and interpret fMRI responses, some of these features need to be  
33 known. This is important in order to model their effect and interpret the results in the  
34 light of their respective signal biases (Gagnon et al., 2015; Heinzle et al., 2015;  
35 Markuerkiaga et al., 2016).

36 In BOLD fMRI, variations in the venous baseline blood volume can be problematic. For  
37 instance, due to the flow of diluted deoxy-hemoglobin concentrations, large veins that  
38 are passing through the upper cortical layers can evoke signal changes distant to the

1 source of the concentration changes. Hence, layer-dependent variations of venous  
2 baseline CBV can be considered as a scaling parameter of locally-unspecific functional  
3 signal changes (Guidi et al., 2016).

4 Since VASO is a quantitative contrast that provides local volume results in physical  
5 units of ml, it is believed to be less biased towards variations in the vessel structure.  
6 Even though there are layer-dependent variations in baseline CBV (see Fig. 6 **(G)**-**(H)**  
7 and (Duvernoy et al., 1981; Weber et al., 2008)), the mere presence of blood vessels  
8 does not mean that they introduce a CBV fMRI signal confound during the functional  
9 task, like they do in BOLD fMRI. Layer-dependent variations of baseline CBV can be  
10 considered as spatially-varying the dynamic range of fMRI responses to the average  
11 neural metabolism within each layers.

12 Aside of potential biases with respect to variations in baseline vasculature, there is a  
13 biological limit of mapping neural activity by means of the hemodynamic response.  
14 For microvessels across cortical columns, the spatial limit of neurovascular coupling is  
15 in the range of the inter-columnar distance of  $\approx 0.5$  mm (Blinder et al., 2013). The  
16 vascular organization across the cortical depth, however, may be less specific. CBV  
17 signal changes in ultra-high resolution animal fMRI is often suggested to be arising  
18 from layer-specific micovessels only (Harel et al., 2006; Zhao et al., 2007). Optical  
19 studies, however, report of CBV contributions of layer-unspecific diving arterioles  
20 (Tian et al., 2010) up to large pial arteries (Kennerley et al., 2012). While their effect  
21 on layer-dependent fMRI responses are considered to be much smaller compared to  
22 the BOLD signal (Huber et al., 2015b), it has not been conclusively established up to  
23 what extent macrovascular CBV contaminations might contribute to layer-dependent  
24 CBV fMRI results (Huber et al., 2015a).

#### 25 **4.7. Neuroscientific layer-dependent applications**

26 This study focuses on tackling the technical challenges that need to be met in order to  
27 obtain interpretable layer-dependent fMRI responses, and as such, a detailed  
28 explanation of the finger-tapping-induced signal in light of neural feed-forward/feed-  
29 back circuitry (Weiler et al., 2008) is beyond the scope of this paper. Nevertheless, we  
30 shall assess the possibility of layer-dependent interpretation with the presented  
31 results.

32 There are three major challenges in inferring neuroscientific interpretations from high-  
33 resolution fMRI data:

34 **4.7.1. Resolution-sensitivity compromise:** In animal studies resolutions up to few  
35 hundred  $\mu\text{m}$  fMRI can be routinely achieved. This can provide layer-specific  
36 responses within individual cortical layers. In human layer-dependent fMRI  
37 studies, however, currently achievable resolutions of 0.75 - 0.8 mm are just

1 beginning to unravel groups of cortical layers without considerable partial  
2 voluming from CSF or WM. Hence, special care must be taken in order to get  
3 even near the resolution of the nominal voxel size. Here, degradation in the  
4 effective resolution is sought to be kept as low as possible by minimizing the  
5 partial Fourier-factor and  $T_2^*$ -related image blurring (Huber et al., 2015c) as  
6 well as by avoiding signal interpolation during image registration (Renvall et al.,  
7 2016).

8 The achievable resolution and voxel size of the fMRI acquisition is not only  
9 limited by the amount of MRI signal available to detect functional activations in  
10 the first place, but mostly by the available gradient power, corresponding  
11 acquisition speed and constraints of peripheral nerve stimulations. Hence, even  
12 with the high SNR of multi-channel coil arrays and application of advanced  
13 acceleration methods, additional challenge remains to acquire the signal in a  
14 useful time scale - preferably smaller than the tissue's  $T_2^*$ . In the experiments  
15 described here, this challenge could be addressed by partly sacrificing the  
16 flexibility regarding the FOV dimensions and using slice orientation  
17 perpendicular to the cortical surface.

18 We would also like to stress that the the protocol used here is kept within the  
19 parameter space of most 7 T fMRI studies. The total fMRI experiment duration  
20 was only 12 min and, therefore, much shorter than most protocols to detect  
21 layer-dependent activity. Furthermore, no custom designed scanner hardware  
22 was used.

23 **4.7.2. Accuracy of layer-dependent analysis:** The interpretation of layer-dependent  
24 results averaged over large areas of cortex relies on accurate post-processing  
25 including: creation of an accurate surface model, cortical depth estimation,  
26 distortion correction etc. For example, the application of so-called 'anatomical  
27 sequences', as an anatomical reference with a readouts that are non-distortion  
28 matched to the fMRI data, can result in signal smoothing across the cortical  
29 depth (Huber et al., 2016b; Renvall et al., 2016). Analogously, imperfections in  
30 distortion corrections and signal interpolation during coregistration will result  
31 in loss of spatial specificity. Furthermore, inaccurate algorithms used for the  
32 estimation the cortical depth can 'introduce' spurious fMRI peaks into cortical  
33 profiles that are not really there (Waehnert et al., 2014).

34 In the study presented here, a strong effort was made to avoid such pitfalls by  
35 improving the functional sensitivity to an extent that layer-dependent  
36 responses can be seen in single-slice functional maps, without relying on  
37 extensive signal averaging over large chunks of cortex. By performing all signal  
38 evaluation directly in EPI space, distortion correction and coregistration are

1 rendered unnecessary. Hence, the results shown in Fig. 6. are largely  
2 unaffected by inaccurate post-processing.

3 Based on the considerations above, we conclude that 3D-segmented-EPI VASO  
4 provides a promising sequence for neuroscientific studies that use layer-  
5 dependent analysis.

#### 6 **4.8. Other fMRI contrast mechanisms**

7 Spin-echo BOLD fMRI has been suggested to have higher specificity to the  
8 microvasculature (Bandettini et al., 1994; Uludag et al., 2009) and its utility for laminar  
9 fMRI has been demonstrated in animals (Goense et al., 2012b; Harel et al., 2006; Zhao  
10 et al., 2006) and in humans (Yacoub et al., 2005). Until today SE-BOLD has been the  
11 only fMRI method to directly map orientation columns in human visual cortex (Yacoub  
12 et al., 2008). However, it suffers from much lower sensitivity, especially at high  
13 resolution (Boyacioglu et al., 2014; Budde et al., 2014; Harmer et al., 2012) and  
14 practical constraints posed by RF power deposition, which may limit the widespread  
15 application of the technique. Future studies with a direct comparison of functional  
16 specificity of VASO CBV and SE-BOLD are required to assess their applicability to  
17 address neuroscientific layer-dependent questions.

#### 18 **4.9. Other readout strategies.**

19 There have been alternative readout strategies proposed to increase the imaging  
20 coverage beside 3D-segmented-EPI. For instance, VASO has been combined with  
21 imaging readouts including 3D-GRASE, (Lu et al., 2004; Poser and Norris, 2011, 2009),  
22 TFL/FFE (Cheng et al., 2014b; Hua et al., 2013), and 3D-HASTE (Poser and Norris,  
23 2007). These 3D-based readout strategies also have the potential of advanced  
24 acceleration in both phase-encoding directions with potential CAIPI field-of-view  
25 shifting. At high resolutions, however, the readout methods of 3D-GRASE and 3D-  
26 HASTE are partly limited by the long readout duration compared to the tissue's  $T_2$ ,  
27 which can result in signal blurring along the second phase-encoding direction (Kemper  
28 et al., 2015). Multi-shot, fast GRE readout methods (TFL/FFE), such as used in (Cheng  
29 et al., 2014b; Hua et al., 2013), do not have this limitation and could be a promising  
30 alternative for 3D-segmented-EPI-VASO at high resolutions. The contrast independent  
31 signal acquisition with a fast GRE readout might not only be a suitable approach in  
32 combination with VASO imaging (Hua et al., 2013). Encouraging results have also been  
33 shown in the elegant combination of a T2-prep module with a fast GRE readout (Hua  
34 et al., 2014). Future studies are needed to investigate the functional contrast of this  
35 approach compared to VASO at high spatial resolutions.

#### 36 **5. Conclusion**

1 Our results show that for neuroscientific layer-dependent applications, it may be more  
2 helpful to refrain from conventional functional contrast (GE-BOLD) and readout  
3 strategies (2D-EPI). The challenges of ultra-high resolutions can be optimally addressed  
4 with alternative and not yet widespread contrast mechanisms (e.g. CBV) and readout  
5 strategies (e.g. 3D-segmented-EPI).

## 6 **6. Acknowledgements**

7 We thank Puja Panwar, Benjamin Gutierrez, and Kenny Chung for radiographic  
8 assistance. We thank Steve Cauley at MGH for sharing the interface of their image  
9 reconstruction for use with the SMS acquisition. The research was supported by the  
10 NIMH Intramural Research Program (#ZIA-MH002783). The study was approved under  
11 NIH Combined Neuroscience Institutional Review Board protocol #93-M-0170  
12 (ClinicalTrials.gov identifier: NCT00001360). Co-authors contributions were supported  
13 by Netherlands Organization for Scientific Research NWO: VIDI 452-11-002 for Kamil  
14 Uludağ and Initial Training Network, HiMR, funded by the FP7 Marie Curie Actions of  
15 the European Commission (FP7-PEOPLE-2012-ITN-316716) for Maria Guidi. Many  
16 thanks to Jozien Goense for continuously consulting us regarding layer-dependent  
17 fMRI. We thank Carsten Stueber for providing us the histology slice shown in Fig. 6. We  
18 acknowledge Harald Möller for early suggestion to combine VASO with a 3D-EPI  
19 readout. The 3D-EPI sequence code used here is based on previously published 3D-EPI  
20 sequences (Poser et al., 2010), and we would like to thank Markus Barth for his  
21 contributions to earlier versions of this sequence. We also want to thank Eric Wong for  
22 discussions about the mechanisms, where the SNR increase in 3D-acquisitions is  
23 coming from. The authors are happy to share the sequence upon request. Preliminary  
24 accounts of this work have been presented in the Proceedings of the 24th Annual  
25 Meeting of ISMRM, Singapore, 2016 (abstract 944).

## 26 **7. References**

- 27 Bandettini, P.A., Wong, E.C., Jesmanowicz, A., Hinks, R.S., Hyde, J.S., 1994. Spin-echo and  
28 gradient-echo EPI of human brain activation using BOLD contrast: a comparative study  
29 at 1.5 T. *NMR Biomed.* 7, 12–20. doi:10.1002/nbm.1940070104
- 30 Blinder, P., Tsai, P.S., Kaufhold, J.P., Knutsen, P.M., Suhl, H., Kleinfeld, D., 2013. The cortical  
31 angiome: an interconnected vascular network with noncolumnar patterns of blood  
32 flow. *Nat. Neurosci.* 16, 889–897. doi:10.1038/nn.3426
- 33 Boyacioglu, R., Schulz, J., Müller, N.C.J., Koopmans, P.J., Barth, M., Norris, D.G., 2014. Whole  
34 brain, high resolution multiband spin-echo EPI fMRI at 7T: A comparison with gradient-  
35 echo EPI using a color-word Stroop task. *Neuroimage* 97, 142–150.  
36 doi:10.1016/j.neuroimage.2014.04.011
- 37 Budde, J., Shajan, G., Zaitsev, M., Scheffler, K., Pohmann, R., 2014. Functional MRI in human  
38 subjects with gradient-echo and spin-echo EPI at 9.4 T. *Magn. Reson. Med.* 71, 209–

1           218. doi:10.1002/mrm.24656

2   Cauley, S.F., Polimeni, J.R., Bhat, H., Wald, L.L., Setsompop, K., 2014. Interslice leakage  
3        artifact reduction technique for simultaneous multislice acquisitions. *Magn. Reson.*  
4        *Med.* 72, 93–102. doi:10.1002/mrm.24898

5   Cheng, Y., van Zijl, P.C.M., Hua, J., 2014a. Measurement of parenchymal extravascular R2\*  
6        and tissue oxygen extraction fraction using multi-echo vascular space occupancy MRI at  
7        7T. *NMR Biomed.* 28, 264–271. doi:10.1002/nbm.3250

8   Cheng, Y., van Zijl, P.C.M., Pekar, J.J., Hua, J., 2014b. Three-dimensional acquisition of  
9        cerebral blood volume and flow responses during functional stimulation in a single  
10        scan. *Neuroimage* 103, 533–541. doi:10.1016/j.neuroimage.2014.08.025

11   Cox, R., 1996. AFNI: Software for analysis and visualization of functional magnetic resonance  
12        neuroimages. *Comput Biomed Res* 29, 162–173. doi:10.1006/cbmr.1996.0014

13   Donahue, M.J., Hoogduin, H., van Zijl, P.C.M., Jezard, P., Luijten, P.R., Hendrikse, J., 2010.  
14        Blood oxygenation level-dependent (BOLD) total and extravascular signal changes and  
15         $\Delta R2^*$  in human visual cortex at 1.5, 3.0 and 7.0 T. *NMR Biomed.* 24, 25–34.  
16        doi:10.1002/nbm.1552

17   Donahue, M.J., Stevens, R.D., de Boorder, M., Pekar, J.J., Hendrikse, J., van Zijl, P.C.M., 2009.  
18        Hemodynamic changes after visual stimulation and breath holding provide evidence for  
19        an uncoupling of cerebral blood flow and volume from oxygen metabolism. *J. Cereb.*  
20        *Blood Flow Metab.* 29, 176–185. doi:10.1038/jcbfm.2008.109

21   Duvernoy, H.M., Delon, S., Vannson, J.L., 1981. Cortical blood vessels of the human brain.  
22        *Brain Res.* 7, 519–579. doi:10.1016/0361-9230(81)90007-1

23   Engel, S.A., Glover, G.G., Wandell, B.A., 1997. Retinotopic organization in human visual cortex  
24        and the spatial precision of functional MRI. *Cereb Cortex* 7, 181–192.  
25        doi:10.1093/cercor/7.2.181

26   Feinberg, D.A., Beckett, A., Chen, L., 2013. Arterial spin labeling with simultaneous multi-  
27        slice echo planar imaging. *Magn. Reson. Med.* 70, 1500–1506. doi:10.1002/mrm.24994

28   Feinberg, D.A., Setsompop, K., 2013. Ultra-fast MRI of the human brain with simultaneous  
29        multi-slice imaging. *J. Magn. Reson.* 229, 90–100. doi:10.1016/j.jmr.2013.02.002

30   Feinberg, D. a, Moeller, S., Smith, S.M., Auerbach, E.J., Ramanna, S., Gunther, M., Glasser,  
31        M.F., Miller, K.L., Uludag, K., Yacoub, E., 2010. Multiplexed echo planar imaging for sub-  
32        second whole brain fMRI and fast diffusion imaging. *PLoS One* 5, e15710.  
33        doi:10.1371/journal.pone.0015710

34   Gagnon, L., Sakadzic, S., Lesage, F., Musacchia, J.J., Lefebvre, J., Fang, Q., Yucel, M. a., Evans,  
35        K.C., Mandeville, E.T., Cohen-Adad, J., Polimeni, J.R., Yaseen, M.A., Lo, E.H., Greve, D.N.,  
36        Buxton, R.B., Dale, a. M., Devor, A., Boas, D.A., 2015. Quantifying the microvascular  
37        origin of BOLD-fMRI from first principles with two-photon microscopy and an oxygen-  
38        sensitive nanoprobe. *J. Neurosci.* 35, 3663–3675. doi:10.1523/JNEUROSCI.3555-  
39        14.2015

- 1 Gai, N.D., Talagala, S.L., Butman, J. a., 2011. Whole-brain cerebral blood flow mapping using  
2 3D echo planar imaging and pulsed arterial tagging. *J. Magn. Reson. Imaging* 33, 287–  
3 295. doi:10.1002/jmri.22437
- 4 Glielmi, C.B., Schuchard, R.A., Hu, X.P., 2009. Estimating cerebral blood volume with  
5 expanded vascular space occupancy slice coverage. *Magn. Reson. Med.* 61, 1193–1200.  
6 doi:10.1002/mrm.21979
- 7 Glover, G.H., Lai, S., 1998. Self-navigated spiral fMRI: Interleaved versus single-shot. *Magn.*  
8 *Reson. Med.* 39, 361–368. doi:10.1002/mrm.1910390305
- 9 Goense, J.B.M., Bohraus, Y., Logothetis, N.K., 2016. fMRI at high spatial resolution:  
10 Implications for BOLD-models. *Front. Comput. Neurosci.* 10, 1–13.  
11 doi:10.3389/fncom.2016.00066
- 12 Goense, J.B.M., Merkle, H., Logothetis, N.K., 2012a. High-resolution fMRI reveals laminar  
13 differences in neurovascular coupling between positive and negative BOLD responses.  
14 *Neuron* 76, 629–639. doi:10.1016/j.neuron.2012.09.019
- 15 Goense, J.B.M., Whittingstall, K., Logothetis, N.K., 2012b. Neural and BOLD responses across  
16 the brain. *Wiley Interdiscip. Rev. Cogn. Sci.* 3, 75–86. doi:10.1002/wcs.153
- 17 Goense, J.B.M., Zappe, A.-C., Logothetis, N.K., 2007. High-resolution fMRI of macaque V1.  
18 *Magn. Reson. Imaging* 25, 740–747. doi:10.1016/j.mri.2007.02.013
- 19 Grgac, K., van Zijl, P.C.M., Qin, Q., 2012. Hematocrit and oxygenation dependence of blood  
20 H<sub>2</sub>O T<sub>1</sub> at 7 tesla. *Magn. Reson. Med.* 70, 1153–1159. doi:10.1002/mrm.24547
- 21 Griswold, M. a, Breuer, F., Blamire, A.M., Kannengiesser, S., Heidemann, R.M., Mueller, M.,  
22 Nittka, M., Jellus, V., Kiefer, B., Jakob, P.M., 2006. Autocalibrated coil sensitivity  
23 estimation for parallel imaging. *NMR Biomed.* 19, 316–24. doi:10.1002/nbm.1048
- 24 Guidi, M., Huber, L., Lampe, L., Gauthier, C.J., Möller, H.E., 2016. Lamina-dependent  
25 calibrated BOLD response in human primary motor cortex. *Neuroimage* ahead of print.  
26 doi:10.1016/j.neuroimage.2016.06.030
- 27 Haacke, E.M., Lindsogkj, E.D., Lin, W., 1991. A fast, iterative, partial-fourier technique  
28 capable of local phase recovery. *J. Magn. Reson.* 92, 126–145. doi:10.1016/0022-  
29 2364(91)90253-P
- 30 Hales, P.W., Kirkham, F.J., Clark, C.A., 2015. A general model to calculate the spin-lattice (T<sub>1</sub>)  
31 relaxation time of blood, accounting for haematocrit, oxygen saturation and magnetic  
32 field strength. *J. Cereb. Blood Flow Metab.* 36, 370–374.  
33 doi:10.1177/0271678X15605856
- 34 Harel, N., Lin, J., Moeller, S., Ugurbil, K., Yacoub, E., 2006. Combined imaging-histological  
35 study of cortical laminar specificity of fMRI signals. *Neuroimage* 29, 879–887.  
36 doi:10.1016/j.neuroimage.2005.08.016
- 37 Harmer, J., Sanchez-Panchuelo, R.M., Bowtell, R.W., Francis, S.T., 2012. Spatial location and  
38 strength of BOLD activation in high-spatial-resolution fMRI of the motor cortex: A

- 1 comparison of spin echo and gradient echo fMRI at 7 T. *NMR Biomed.* 25, 717–25.  
2 doi:10.1002/nbm.1783
- 3 Heinzle, J., Koopmans, P.J., den Ouden, H.E., Ramanna, S., Klaas, S.E., 2015. A hemodynamic  
4 model for layered BOLD signals 125, 556–570. doi:10.1016/j.neuroimage.2015.10.025
- 5 Hua, J., Jones, C.K., Qin, Q., van Zijl, P.C.M., 2013. Implementation of vascular-space-  
6 occupancy MRI at 7T. *Magn. Reson. Med.* 69, 1003–1013. doi:10.1002/mrm.24334
- 7 Hua, J., Qin, Q., van Zijl, P.C.M., Pekar, J.J., Jones, C.K., 2014. Whole-brain three-dimensional  
8 T2-weighted BOLD functional magnetic resonance imaging at 7 Tesla. *Magn. Reson.*  
9 *Med.* 72, 1530–1540. doi:10.1002/mrm.25055
- 10 Huber, L., Goense, J.B.M., Kennerley, A.J., Guidi, M., Trampel, R., Turner, R., Möller, H.E.,  
11 2015a. Micro- and macrovascular contributions to layer-dependent blood blood  
12 volume fMRI: A multi-modal, multi-species comparison, in: *Proceedings of the*  
13 *International Society of Magnetic Resonance in Medicine.* p. 2114.
- 14 Huber, L., Goense, J.B.M., Kennerley, A.J., Ivanov, D., Krieger, S.N., Lepsien, J., Trampel, R.,  
15 Turner, R., Möller, H.E., 2014a. Investigation of the neurovascular coupling in positive  
16 and negative BOLD responses in human brain at 7T. *Neuroimage* 97, 349–362.  
17 doi:10.1016/j.neuroimage.2014.04.022
- 18 Huber, L., Goense, J.B.M., Kennerley, A.J., Trampel, R., Guidi, M., Ivanov, D., Gauthier, C.J.,  
19 Turner, R., Möller, H.E., 2015b. Cortical lamina-dependent blood volume changes in  
20 human brain at 7 T. *Neuroimage* 107, 23–33. doi:10.1016/j.neuroimage.2014.11.046
- 21 Huber, L., Guidi, M., Goense, J.B.M., Mildner, T., Trampel, R., Schulz, J., Eichner, C., Turner,  
22 R., Möller, H.E., 2015c. The magnitude point spread function is an inadequate measure  
23 of T2\*-blurring in EPI, in: *Proceedings of the International Society of Magnetic*  
24 *Resonance in Medicine.* p. 2056.
- 25 Huber, L., Ivanov, D., Guidi, M., Turner, R., Uludag, K., Möller, H.E., Poser, B.A., 2016a.  
26 Functional cerebral blood volumemapping with simultaneous multi-slice acquisition.  
27 *Neuroimage* 125, 1159–1168. doi:10.1016/j.neuroimage.2015.10.082
- 28 Huber, L., Ivanov, D., Krieger, S.N., Streicher, M.N., Mildner, T., Poser, B.A., Möller, H.E.,  
29 Turner, R., 2014b. Slab-selective, BOLD-corrected VASO at 7 tesla provides measures of  
30 cerebral blood volume reactivity with high signal-to-noise ratio. *Magn. Reson. Med.* 72,  
31 137–148. doi:10.1002/mrm.24916
- 32 Huber, L., Marrett, S., Handwerker, D.A., Thomas, A., Gutierrez, B., Ivanov, D., Poser, B.A.,  
33 Bendettini, P.A., 2016b. Fast dynamic measurement of functional T1 and grey matter  
34 thickness changes during brain activation at 7T, in: *Proceedings of the International*  
35 *Society of Magnetic Resonance in Medicine.* p. 633.
- 36 Hurley, A.C., Al-Radaideh, A., Bai, L., Aickelin, U., Coxon, R., Glover, P., Gowland, P.A., 2010.  
37 Tailored RF pulse for magnetization inversion at ultrahigh field. *Magn. Reson. Med.* 63,  
38 51–58. doi:10.1002/mrm.22167
- 39 Ivanov, D., Barth, M., Uludag, K., Poser, B.A., 2015. Robust ACS acquisition for 3D echo



- 1 planar imaging, in: Proceedings of the International Society of Magnetic Resonance in  
2 Medicine. p. 2059.
- 3 Ivanov, D., Poser, B.A., Huber, L., Pfeuffer, J., Uludağ, K., 2016a. Optimization of  
4 simultaneous multislice EPI for concurrent functional perfusion and BOLD signal  
5 measurements at 7T. *Magn. Reson. Med.* doi:10.1002/mrm.26351
- 6 Ivanov, D., Poser, B.A., Kashyap, S.S., Gardumi, A., Huber, L., Uludag, K., 2016b. Sub-  
7 millimeter human brain perfusion, in: Proceedings of the High Field Meeting of the  
8 International Society of Magnetic Resonance in Medicine. p. 14.
- 9 Jesmanowicz, A., Bandettini, P.A., Hyde, J.S., 1998. Single-shot half k-space high-resolution  
10 gradient-recalled EPI for fMRI at 3 tesla. *Magn. Reson. Med.* 40, 754–762.
- 11 Jin, T., Kim, S.-G., 2006. Spatial dependence of CBV-fMRI: a comparison between VASO and  
12 contrast agent based methods., in: Conference Proceedings of the IEEE Engineering in  
13 Medicine and Biology Society. pp. 25–28. doi:10.1109/IEMBS.2006.259553
- 14 Jorge, J., Figueiredo, P., van der Zwaag, W., Marques, J., 2013. Signal fluctuations in fMRI  
15 data acquired with 2D-EPI and 3D-EPI at 7 Tesla. *Magn. Reson. Imaging* 31, 212–220.  
16 doi:10.1016/j.mri.2012.07.001
- 17 Kazan, S.M., Mohammadi, S., Callaghan, M.F., Flandin, G., Huber, L., Leech, R., Kennerley, A.,  
18 Windischberger, C., Weiskopf, N., 2015. Vascular Autorescaling of fMRI (VasA fMRI)  
19 Improves Sensitivity of Population Studies: A Pilot Study. *Neuroimage*.  
20 doi:10.1016/j.neuroimage.2015.09.033
- 21 Kemper, V.G., De Martino, F., Yacoub, E., Goebel, R., 2015. Variable flip angle 3D-GRASE for  
22 high resolution fMRI at 7 tesla. *Magn. Reson. Med.* 0, n/a-n/a. doi:10.1002/mrm.25979
- 23 Kennerley, A.J., Harris, S., Bruyns-Haylett, M., Boorman, L., Zheng, Y., Jones, M., Berwick, J.,  
24 2012. Early and late stimulus-evoked cortical hemodynamic responses provide insight  
25 into the neurogenic nature of neurovascular coupling. *J. Cereb. Blood Flow Metab.* 32,  
26 468–480. doi:10.1038/jcbfm.2011.163
- 27 Kim, S.-G., Harel, N., Jin, T., Kim, T., Lee, P., Zhao, F., 2013. Cerebral blood volume MRI with  
28 intravascular superparamagnetic iron oxide nanoparticles. *NMR Biomed.* 26, 949–962.  
29 doi:10.1002/nbm.2885
- 30 Kim, S.-G., Ogawa, S., 2012. Biophysical and physiological origins of blood oxygenation level-  
31 dependent fMRI signals. *J. Cereb. Blood Flow Metab.* 32, 1188–1206.  
32 doi:10.1038/jcbfm.2012.23
- 33 Kim, T., Shin, W., Zhao, T., Beall, E.B., Lowe, M.J., Bae, K.T., 2013. Whole brain perfusion  
34 measurements using arterial spin labeling with multiband acquisition. *Magn. Reson.*  
35 *Med.* 70, 1653–1661. doi:10.1002/mrm.24880
- 36 Koopmans, P.J., Barth, M., Norris, D.G., 2010. Layer-specific BOLD activation in human V1.  
37 *Hum. Brain Mapp.* 31, 1297–1304.
- 38 Koopmans, P.J., Barth, M., Orzada, S., Norris, D.G., 2011. Multi-echo fMRI of the cortical

- 1 laminae in humans at 7 T. *Neuroimage* 56, 1276–1285.  
2 doi:10.1016/j.neuroimage.2011.02.042
- 3 Ladstein, J., Evensmoen, H.R., Haberg, A.K., Kristoffersen, A., Goa, P.E., 2016. Effect of Task-  
4 Correlated Physiological Fluctuations and Motion in 2D and 3D Echo-Planar Imaging in  
5 a Higher Cognitive Level fMRI Paradigm. *Front. Neurosci.* 10, Article 225.  
6 doi:10.3389/fnins.2016.00225
- 7 Langkammer, C., Bredies, K., Poser, B. a., Barth, M., Reishofer, G., Fan, A.P., Bilgic, B.,  
8 Fazekas, F., Mainero, C., Ropele, S., 2015. Fast quantitative susceptibility mapping using  
9 3D EPI and total generalized variation. *Neuroimage* 111, 622–630.  
10 doi:10.1016/j.neuroimage.2015.02.041
- 11 Larkman, D.J., Hajnal, J. V., Herlihy, A.H., Coutts, G.A., Young, I.R., Ehnholm, G., 2001. Use of  
12 multicoil arrays for separation of signal from multiple slices simultaneously excited. *J.*  
13 *Magn. Reson. Imaging* 13, 313–317. doi:10.1002/1522-2586(200102)13:2<313::AID-  
14 JMRI1045>3.0.CO;2-W
- 15 Lu, H., Golay, X., Pekar, J.J., van Zijl, P.C.M., 2003. Functional magnetic resonance imaging  
16 based on changes in vascular space occupancy. *Magn. Reson. Med.* 50, 263–274.  
17 doi:10.1002/mrm.10519
- 18 Lu, H., van Zijl, P.C.M., 2012. A review of the development of vascular-space-occupancy  
19 (VASO) fMRI. *Neuroimage* 62, 736–742. doi:10.1016/j.neuroimage.2012.01.013
- 20 Lu, H., van Zijl, P.C.M., 2005. Experimental measurement of extravascular parenchymal  
21 BOLD effects and tissue oxygen extraction fractions using multi-echo VASO fMRI at 1.5  
22 and 3.0 T. *Magn. Reson. Med.* 53, 808–816. doi:10.1002/mrm.20379
- 23 Lu, H., van Zijl, P.C.M., Hendrikse, J., Golay, X., 2004. Multiple acquisitions with global  
24 inversion cycling (MAGIC): a multislice technique for vascular-space-occupancy  
25 dependent fMRI. *Magn. Reson. Med.* 51, 9–15. doi:10.1002/mrm.10659
- 26 Lutti, A., Thomas, D.L., Hutton, C., Weiskopf, N., 2013. High-resolution functional MRI at 3 T:  
27 3D/2D echo-planar imaging with optimized physiological noise correction. *Magn.*  
28 *Reson. Med.* 69, 1657–1664. doi:10.1002/mrm.24398
- 29 Mansfield, P., Coxon, R., Hyklin, J., 1995. Echo-volumar imaging (EVI) of the brain at 3.0 T:  
30 first normal volunteer and functional imaging results. *J. Comput. Assist. Tomogr.* 19,  
31 847–852.
- 32 Markuerkiaga, I., Barth, M., Norris, D.G., 2016. A cortical vascular model for examining the  
33 specificity of the laminar BOLD signal. *Neuroimage* 132, 491–498.  
34 doi:10.1016/j.neuroimage.2016.02.073
- 35 Marques, J.P., Kober, T., Krueger, G., van der Zwaag, W., Van de Moortele, P.-F., Gruetter,  
36 R., 2010. MP2RAGE, a self bias-field corrected sequence for improved segmentation  
37 and T1-mapping at high field. *Neuroimage* 49, 1271–1281.  
38 doi:10.1016/j.neuroimage.2009.10.002
- 39 Menon, R., Ogawa, S., Strupp, J., Anderson, P., Ugurbil, K., 1995. BOLD based functional MRI

- 1 at 4 tesla includes a capillary bed contribution: echo-planar imaging correlates with  
2 previous optical imaging using intrinsic signal. *Magn Reson Med* 33, 453–459.  
3 doi:10.1002/mrm.1910330323
- 4 Mildner, T., Müller, K., Hetzer, S., Trampel, R., Driesel, W., Möller, H.E., 2014. Mapping of  
5 arterial transit time by intravascular signal selection. *NMR Biomed.* 27, 594–609.  
6 doi:10.1002/nbm.3098
- 7 Moeller, S., Yacoub, E., Olman, C. a, Auerbach, E., Strupp, J., Harel, N., Ugurbil, K., 2010.  
8 Multiband multislice GE-EPI at 7 tesla, with 16-fold acceleration using partial parallel  
9 imaging with application to high spatial and temporal whole-brain fMRI. *Magn. Reson.*  
10 *Med.* 63, 1144–1153. doi:10.1002/mrm.22361
- 11 Murphy, K., Bodurka, J., Bandettini, P.A., 2007. How long to scan? The relationship between  
12 fMRI temporal signal to noise ratio and necessary scan duration. *Neuroimage* 34, 565–  
13 574. doi:10.1016/j.neuroimage.2006.09.032
- 14 Narsude, M., Gallichan, D., van der Zwaag, W., Gruetter, R., Marques, J.P., 2016. Three-  
15 dimensional echo planar imaging with controlled aliasing: A sequence for high  
16 temporal resolution functional MRI. *Magn. Reson. Med.* 75, 2350–2361.  
17 doi:10.1002/mrm.25835
- 18 Polimeni, J.R., Bhat, H., Witzel, T., Benner, T., Feiweier, T., Inati, S.J., Renvall, V., Heberlein,  
19 K., Wald, L.L., 2016. Reducing sensitivity losses due to respiration and motion in  
20 accelerated echo planar imaging by reordering the autocalibration data acquisition.  
21 *Magn. Reson. Med.* 75, 665–679. doi:10.1002/mrm.25628
- 22 Poser, B.A., Ivanov, D., Kannengiesser, S., Uludag, K., Barth, M., 2014. Accelerated 3D EPI  
23 using 2D blipped-CAIPI for high temporal and/or spatial resolution, in: *Proceedings of*  
24 *the International Society of Magnetic Resonance in Medicine.* p. 1506.
- 25 Poser, B.A., Ivanov, D., Kemper, V.G., Kannengiesser, S.A., Uludag, K., Barth, M., 2013.  
26 CAIPIRINHA-accelerated 3D EPI for high temporal and/or spatial resolution EPI  
27 acquisitions, in: *Esmrmb.* p. 226.
- 28 Poser, B.A., Koopmans, P.J., Witzel, T., Wald, L.L., Barth, M., 2010. Three dimensional echo-  
29 planar imaging at 7 tesla. *Neuroimage* 51, 261–266.  
30 doi:10.1016/j.neuroimage.2010.01.108
- 31 Poser, B.A., Norris, D.G., 2011. Application of whole-brain CBV-weighted fMRI to a cognitiv  
32 stimulation paradigm: Robust activation detection in a stroop task experiment using 3D  
33 GRASE VASO. *Hum. Brain Mapp.* 32, 974–981. doi:10.1002/hbm.21083
- 34 Poser, B.A., Norris, D.G., 2009. 3D single-shot VASO using a Maxwell gradient compensated  
35 GRASE sequence. *Magn. Reson. Med.* 62, 255–262. doi:10.1002/mrm.22000
- 36 Poser, B.A., Norris, D.G., 2007. Measurement of activation-related changes in cerebral blood  
37 volume: VASO with single-shot HASTE acquisition. *Magn. Reson. Mater. Physics, Biol.*  
38 *Med.* 20, 63–67. doi:10.1007/s10334-007-0068-0
- 39 Renvall, V., Witzel, T., Wald, L.L., Polimeni, J.R., 2016. Automatic cortical surface

- 1 reconstruction of high-resolution T1 echo planar imaging data. *Neuroimage* 134, 338–  
2 354. doi:10.1016/j.neuroimage.2016.04.004
- 3 Setsompop, K., Gagoski, B. a, Polimeni, J.R., Witzel, T., Wedeen, V.J., Wald, L.L., 2012.  
4 Blipped-controlled aliasing in parallel imaging for simultaneous multislice echo planar  
5 imaging with reduced g-factor penalty. *Magn. Reson. Med.* 67, 1210–1224.  
6 doi:10.1002/mrm.23097
- 7 Smirnakis, S.M., Schmid, M.C., Weber, B., Tolias, A.S., Augath, M., Logothetis, N.K., 2007.  
8 Spatial specificity of BOLD versus cerebral blood volume fMRI for mapping cortical  
9 organization. *J. Cereb. Blood Flow Metab.* 27, 1248–1261.  
10 doi:10.1038/sj.jcbfm.9600434
- 11 Song, A.W., Wong, E.C., Hyde, J.S., 1994. Echo-volume imaging. *Magn. Reson. Med.* 32, 668–  
12 71. doi:10.1002/mrm.1910320518
- 13 Stelzer, J., Lohmann, G., Mueller, K., Buschmann, T., Turner, R., 2014. Deficient approaches  
14 to human neuroimaging. *Front. Hum. Neurosci.* 8, Article 462.  
15 doi:10.3389/fnhum.2014.00462
- 16 Stirnberg, R., Huijbers, W., Poser, B.A., Stocker, T., 2016. Ultra-fast gradient echo EPI with  
17 controlled aliasing at 3T: simultaneous multi-slice vs. 3D-EPI, in: *Proceedings of the*  
18 *International Society of Magnetic Resonance in Medicine.* p. 941.
- 19 Stüber, C., Morawski, M., Schäfer, A., Labadie, C., Wähnert, M., Leuze, C., Streicher, M.N.,  
20 Barapatre, N., Reimann, K., Geyer, S., Spemann, D., Turner, R., 2014. Myelin and iron  
21 concentration in the human brain: A quantitative study of MRI contrast. *Neuroimage*  
22 93, 95–106. doi:10.1016/j.neuroimage.2014.02.026
- 23 Tian, P., Teng, I.C., May, L.D., Kurz, R., Lu, K., Scadeng, M., Hillman, E.M.C., Crespigny, A.J.  
24 De, Arceuil, H.E.D., Mandeville, J.B., Marota, J.J.A., Rosen, B.R., Liu, T.T., Boas, D.A.,  
25 Buxton, R.B., Dale, A.M., Devor, A., 2010. Cortical depth-specific microvascular dilation  
26 underlies laminar differences in blood oxygenation level-dependent functional MRI  
27 signal. *Proc. Natl. Acad. Sci.* 34, 15246–15251. doi:10.1073/pnas.1006735107
- 28 Triantafyllou, C., Polimeni, J.R., Wald, L.L., 2011. Physiological noise and signal-to-noise ratio  
29 in fMRI with multi-channel array coils. *Neuroimage* 55, 597–606.  
30 doi:10.1016/j.neuroimage.2010.11.084
- 31 Turner, R., 2002. How much cortex can a vein drain? Downstream dilution of activation-  
32 related cerebral blood oxygenation changes. *Neuroimage* 16, 1062–1067.  
33 doi:10.1006/nimg.2002.1082
- 34 Uludag, K., Müller-Bierl, B., Ugurbil, K., 2009. An integrative model for neuronal activity-  
35 induced signal changes for gradient and spin echo functional imaging. *Neuroimage* 48,  
36 150–165. doi:10.1016/j.neuroimage.2009.05.051
- 37 van der Zwaag, W., Buur, P., Versluis, M., Marques, J.P., 2016. Distortion-matched T1-maps  
38 and bias-corrected T1w-images as anatomical reference for submillimeter-resolution  
39 fMRI, in: *Proceedings of the International Society of Magnetic Resonance in Medicine.*  
40 p. 1233.

- 1 Van Der Zwaag, W., Marques, J.P., Kober, T., Glover, G., Gruetter, R., Krueger, G., 2012.  
2 Temporal SNR characteristics in segmented 3D-EPI at 7T. *Magn. Reson. Med.* 67, 344–  
3 352. doi:10.1002/mrm.23007
- 4 Waehnert, M.D., Dinse, J., Weiss, M., Streicher, M.N., Waehnert, P., Geyer, S., Turner, R.,  
5 Bazin, P.-L., 2014. Anatomically motivated modeling of cortical laminae. *Neuroimage*  
6 93, 210–220. doi:10.1016/j.neuroimage.2013.03.078
- 7 Weber, B., Keller, A.L., Reichold, J., Logothetis, N.K., 2008. The microvascular system of the  
8 striate and extrastriate visual cortex of the macaque. *Cereb. Cortex* 18, 2318–2330.  
9 doi:10.1093/cercor/bhm259
- 10 Weiler, N., Wood, L., Yu, J., Solla, S.A., Shepherd, G.M.G., 2008. Top-down laminar  
11 organization of the excitatory network in motor cortex. *Nat. Neurosci.* 11, 360–366.  
12 doi:10.1038/nn2049
- 13 Wong, E.C., 2012. Optimized phase schedules for minimizing peak RF power in simultaneous  
14 multi-slice RF excitation pulses, in: *Proceedings of the International Society of Magnetic  
15 Resonance in Medicine.* p. 2209.
- 16 Worsley, K.J., 2001. Statistical analysis of activation images, in: Smith, P.J. and P.M.M. and  
17 S.M. (Ed.), *Functional Magnetic Resonance Imaging: An Introduction to Methods.*  
18 Oxford University Press.
- 19 Wright, P.J., Mougin, O.E., Totman, J.J., Peters, A.M., Brookes, M.J., Coxon, R., Morris, P.E.,  
20 Clemence, M., Francis, S.T., Bowtell, R.W., Gowland, P.A., 2008. Water proton T1  
21 measurements in brain tissue at 7, 3, and 1.5 T using IR-EPI, IR-TSE, and MPRAGE:  
22 Results and optimization. *Magn. Reson. Mater. Physics, Biol. Med.* 21, 121–130.  
23 doi:10.1007/s10334-008-0104-8
- 24 Wu, P., Bandettini, P. a, Harper, R.M., Handwerker, D. a, 2015. Effects of thoracic pressure  
25 changes on MRI signals in the brain. *J. Cereb. Blood Flow Metab.* 35, 1024–1032.  
26 doi:10.1038/jcbfm.2015.20
- 27 Yacoub, E., Harel, N., Ugurbil, K., 2008. High-field fMRI unveils orientation columns in  
28 humans. *Proc. Natl. Acad. Sci.* 105, 10607–106012. doi:10.1073/pnas.0804110105
- 29 Yacoub, E., Ugurbil, K., Harel, N., 2015. fMRI at high magnetic field: Spatial resolution limits  
30 and applications, in: *Brain Mapping: An Encyclopedic Reference.*
- 31 Yacoub, E., Van de Moortele, P.-F., Shmuel, A., Ugurbil, K., 2005. Signal and noise  
32 characteristics of Hahn SE and GE BOLD fMRI at 7 T in humans. *Neuroimage* 24, 738–  
33 750. doi:10.1016/j.neuroimage.2004.09.002
- 34 Zahneisen, B., Ernst, T., Poser, B. a., 2015. SENSE and simultaneous multislice imaging.  
35 *Magn. Reson. Med.* 74, 1356–1362. doi:10.1002/mrm.25519
- 36 Zahneisen, B., Poser, B.A., Ernst, T., Stenger, V.A., 2014. Three-dimensional Fourier encoding  
37 of simultaneously excited slices: Generalized acquisition and reconstruction  
38 framework. *Magn. Reson. Med.* 71, 2071–2081. doi:10.1002/mrm.24875

- 1 Zhao, F., Jin, T., Wang, P., Hu, X., Kim, S.-G., 2007. Sources of phase changes in BOLD and  
2 CBV-weighted fMRI. *Magn. Reson. Med.* 57, 520–527. doi:10.1002/mrm.21159
- 3 Zhao, F., Wang, P., Hendrich, K.S., Uludag, K., Kim, S.-G., 2006. Cortical layer-dependent  
4 BOLD and CBV responses measured by spin-echo and gradient-echo fMRI: Insights into  
5 hemodynamic regulation. *Neuroimage* 30, 1149–1160.  
6 doi:10.1016/j.neuroimage.2005.11.013

7

8 **Figure captions:**

9 **Fig. 1: Magnetization preparation, readout, and sequence timing.**

10 Schematic depiction of one TR in the SS-SI-VASO sequence. **(A)** and **(B)** show the timing of  
11 the most relevant RF and gradient events for 2D-SMS and 3D-segmented-EPI, respectively.  
12 Zoomed views of the corresponding readout modules for individual slices and k-space  
13 segments are depicted in **(D)**-**(E)**. Every TR starts with a ‘global’ adiabatic inversion pulse. A  
14 phase skip is used to control the inversion efficiency and the inflow of fast, un-inverted  
15 blood. The VASO images are acquired around the blood-nulling time at  $T_{I1} = 1.1$  s after  
16 successive application of the multi-band/slab-selective RF excitation pulses for 2D-SMS and  
17 3D acquisitions, respectively. The multi-band factor varies between 1 and 3 in this study  
18 (SMS-factor = 3 in **(D)**). The phase-encoding and read gradients for the acquisition of the  
19 individual slices or k-space segments are accompanied with blipped-CAIPI gradients in  
20 slice/segment-direction for controlled aliasing of nearby slices. In this study the  
21 corresponding FOV-shift factor varied between 1 and 1/3 (FoV-shift = 1/2 in **(D)**-**(E)**). A  
22 second set of images is acquired at  $T_{I2} = 2.6$  s containing BOLD-signal-weighting without  
23 CBV-weighting. Example brain volumes from every readout are depicted next to their RF and  
24 gradient events. Since, the effective TI can vary across slices in the 2D-SMS approach in the  
25 range of 200 ms, clear borders of the individual SMS slabs can be seen from the  
26 corresponding steps in  $T_1$ -weighting (blue arrows in **(A)**).

27 **Fig. 2: tSNR across resolutions.**

28 Results of VASO tSNR for 0.75 mm, 1.5 mm and 3 mm resolutions are shown for one  
29 participant in **(A)**-**(B)**. For the protocols with (low) resolutions of 1.5 mm and 3 mm, 2D-SMS  
30 VASO provides higher tSNR values compared to 3D-segmented-EPI. At sub-millimeter  
31 resolutions of 0.75 mm, however, the tSNR of 3D-segmented-EPI surpasses that of 2D-SMS  
32 EPI. For best visibility, the dynamic range of the color bars is adjusted for each resolution,  
33 but it is kept identical for 2D-SMS and 3D-segmented-EPI. tSNR results in **(C)** refer to  
34 experiments, where slice-acquisition parameters are kept the same but the slice thickness is  
35 varied. Different voxel volumes refer to different slice thicknesses. It can be seen that in the  
36 physiological-noise-dominated regime of voxel volumes with few microliters, 2D-SMS-EPI  
37 performs better than 3D-segmented-EPI. However, in the thermal-noise-dominated regime  
38 at sub-microliters resolutions, 3D-segmented-EPI has higher signal stability. Fig. **(E)**-**(H)** show

1 the same for the BOLD contrast. Similarly to VASO, also the BOLD stability is better for 3D-  
2 segmented-EPI at ultra high resolutions, while 2D-SMS is better for conventional  
3 resolutions. Note that the ceiling effect is slightly stronger in BOLD compared to VASO.  
4 Consequently, the advantage of 3D-segmented-EPI compared to 2D-SMS EPI is visible at  
5 smaller voxel sizes only.

6 All given tSNR/SNR values in **(A)-(C)** and **(E)-(F)** refer to mean values across participants  
7 within ROIs of M1.

8

9 **Fig. 3: Stability of tSNR results across participants.**

10 The higher temporal stability of sub millimeter voxels shown for one representative subject  
11 in Fig. 2 is consistent across participants of the study. For both, BOLD and VASO time series,  
12 tSNR values are higher for 3D-segmented-EPI compared to 2D-EPI. Note that BOLD and  
13 VASO figures are acquired simultaneously, while 3D-segmented-EPI and 2D-EPI figures are  
14 acquired in separate experiments 12 minutes apart. Hence, due to participants head motion  
15 between experiment, the slice position can be minimally different. Since the slice  
16 positioning and slice tilting was adjusted to be perpendicular to the participants individual  
17 M1 cortex, the FOV contains different brain regions for different participants.

18 **Fig. 4: Functional results across resolutions.**

19 Functional activation results for 0.75 mm, 1.5 mm and 3 mm resolutions are shown for one  
20 subject in **(A)-(F)** for 3D-segmented-EPI and **(G)-(L)** for 2D-SMS, respectively. The depicted  
21 participant and the depicted slices are the same as shown in Fig. 2 **(A)-(B)**. For the sake of  
22 comparison, functional maps of BOLD signal changes are shown next to the VASO results.  
23 Note that BOLD signal changes are acquired simultaneously with VASO, while 3D-  
24 segmented-EPI and 2D-SMS data are acquired in two separate experiments  $\approx 14$  min apart.  
25 Also note that the functional contrasts and the color bars are differently optimized across  
26 resolutions, but they are the same for 3D-segmented-EPI and 2D-SMS results. For low  
27 resolutions of 3 mm in **(E)-(F)** and **(K)-(L)**, functional maps don't show strong qualitative  
28 differences for contralateral M1. Independent of contrast and readout-strategy, the high  
29 tSNR values (Fig. 2) result in sensitivities well above the detection threshold in all cases. At  
30 1.5 mm resolution, the higher specificity of CBV-sensitive fMRI starts to pay off. E.g. two  
31 sides of the central sulcus can be better separated with CBV-fMRI compared to BOLD (blue  
32 arrows in **((C)-(D)** and **(I)-(J)**). At 0.75 mm resolution, layer-dependent activity features  
33 become visible in CBV-fMRI results (green arrows in **(A)** and **(G)**), while the BOLD results  
34 appear less specific (green arrows in **(B)** and **(H)**).

35

36 **Fig. 5: Susceptibility to task correlated head motion artefacts**

1 Fig. 5 **(A)** depicts the SPM motion parameter of pitch rotation across one representative 10  
2 min Valsalva experiment. The vertical black bars represent the periods of breathhold. Clear  
3 task correlated motion can be seen. The “sawtooth” pattern between breathholding  
4 periods refers to TR locked paced breathing. Fig. **(B)** and **(C)** show the effect of head tilting  
5 in 2D-SMS VASO and 3D-segmented-EPI VASO. In 2D-SMS VASO, the different effective  
6 inversion time across slices results in different signal intensities. Hence, after retrospective  
7 motion correction (MOCO), this signal discontinuity is resampled into adjacent slices (red  
8 ellipses). This results in task-correlated signal changes visible in the axial plane, rendering  
9 any CBV interpretation impossible. In 3D-segmented-EPI VASO on the other hand, the  
10 homogenous signal intensity allows retrospective motion correction without such  
11 artefacts.

12

### 13 **Fig. 6: Usefulness for layer-dependent applications**

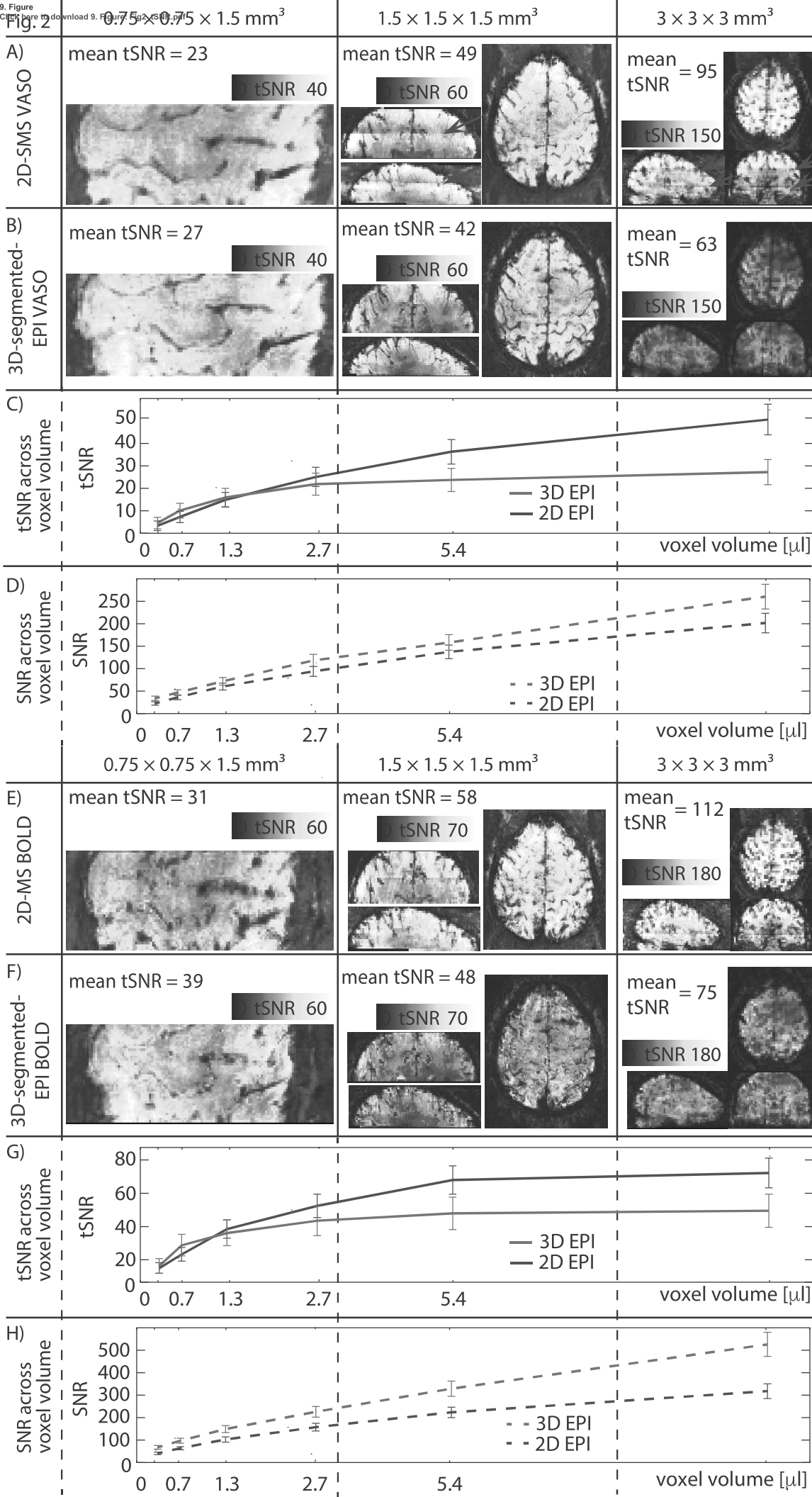
14 fMRI responses across cortical depth. **(A)-(B)** show the section of the functional activity  
15 maps that are used to assess the applicability of VASO and BOLD contrast for layer-  
16 dependent fMRI. **(C)-(D)** depict the cortical profile of VASO and BOLD signal changes across  
17 cortical depth. The VASO signal change appears to be strongest along two cortical depths;  
18 upper cortical layers and deeper cortical layers. In BOLD, a similar pattern can be seen,  
19 however, it is overlaid on top of a strong gradient of largest BOLD signal change above the  
20 cortical surface, decreasing with cortical depth. Data presented in **(A)-(D)** refer to the same  
21 dataset as shown in Fig. 2 **(B)**, **(F)** and Fig. 4 **(G)-(H)**. The approximate position of  
22 cytoarchitectonically defined cortical layers can be given from stained post-mortem tissue  
23 samples (Stüber et al., 2014) (in **(E)** SMI- 311, IHC, cell staining is used). The vertical in this  
24 Fig. are manually overlaid based on the different cell types visible in **(E)**. **(F)** portrays the  
25 collapsed SMI density plotted as a function of cortical depth, i.e. the y-axis refers to the sum  
26 of all gray values within every column of Fig. **(E)**. For most quantitative layer-dependent  
27 activity interpretation, the laminar responses must be considered with respect to the  
28 baseline vasculature. **(G)** presents the micro vessel distribution of M1 as shown in  
29 (Duvernoy et al., 1981). The corresponding baseline CBV is shown in **(H)** as a function of  
30 cortical depth. Data shown in **(H)** are derived as the sum of gray values in columns of Fig.  
31 **(G)**. Data shown in **(E)-(H)** refer to single-subject post mortem samples and correspond to  
32 different individuals as the data acquired in this study **(A)-(D)**.

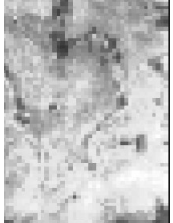
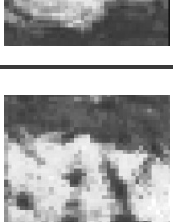
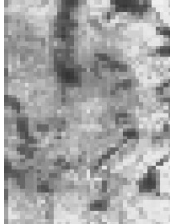
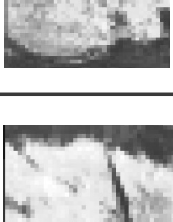

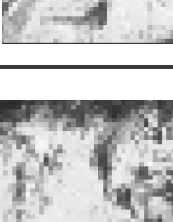

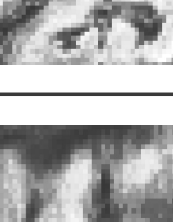

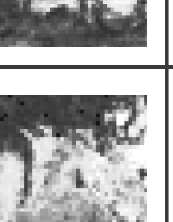


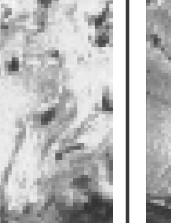
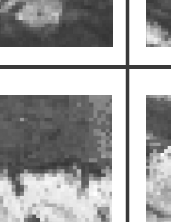
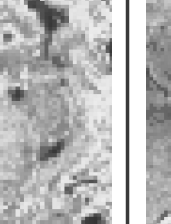

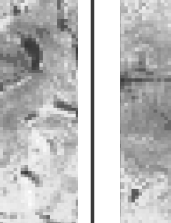

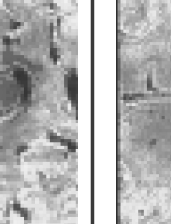

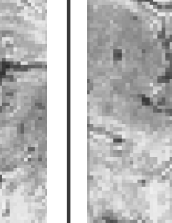

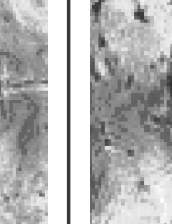
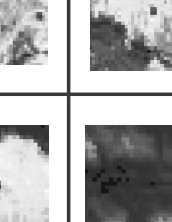




33

34







A) 2D VASO	tSNR 40	tSNR 60	tSNR 60	tSNR 60
from Fig. 2				
remaining participants				
				
				
				
				
				

9. Figure  
 Click here to download 9. Figure: Fig4\_activation.pdf

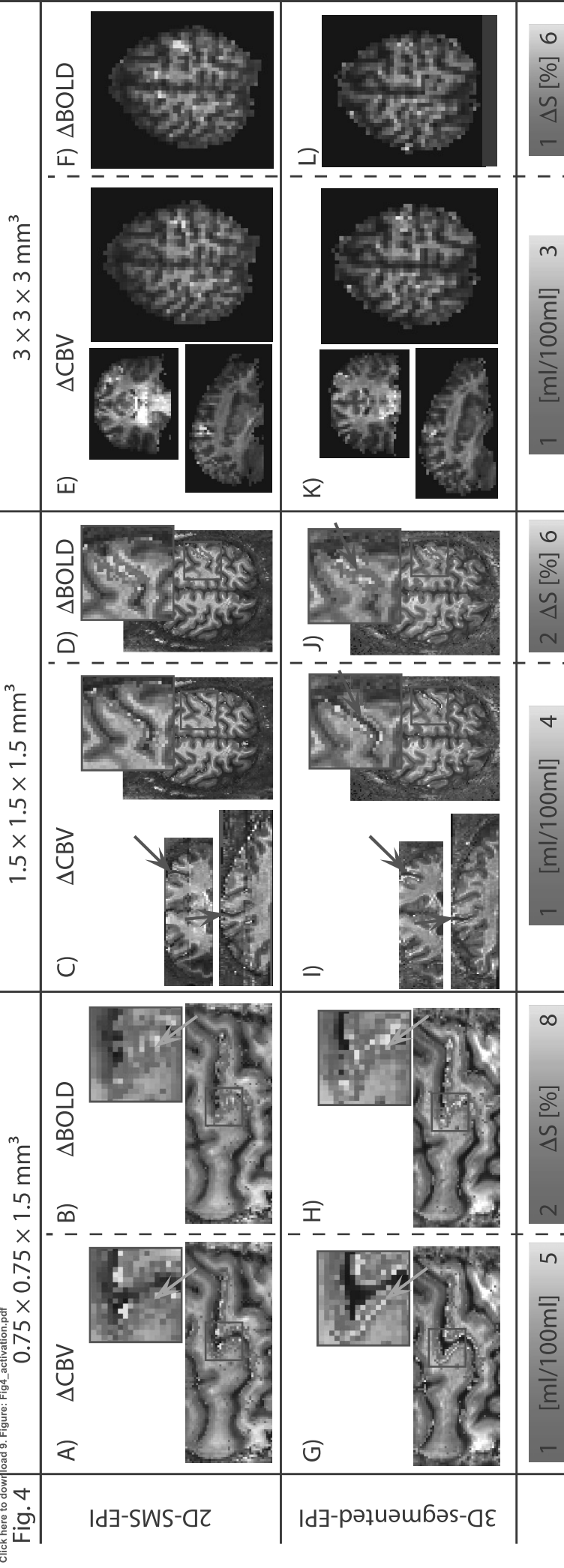
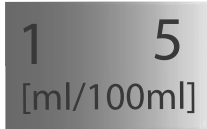


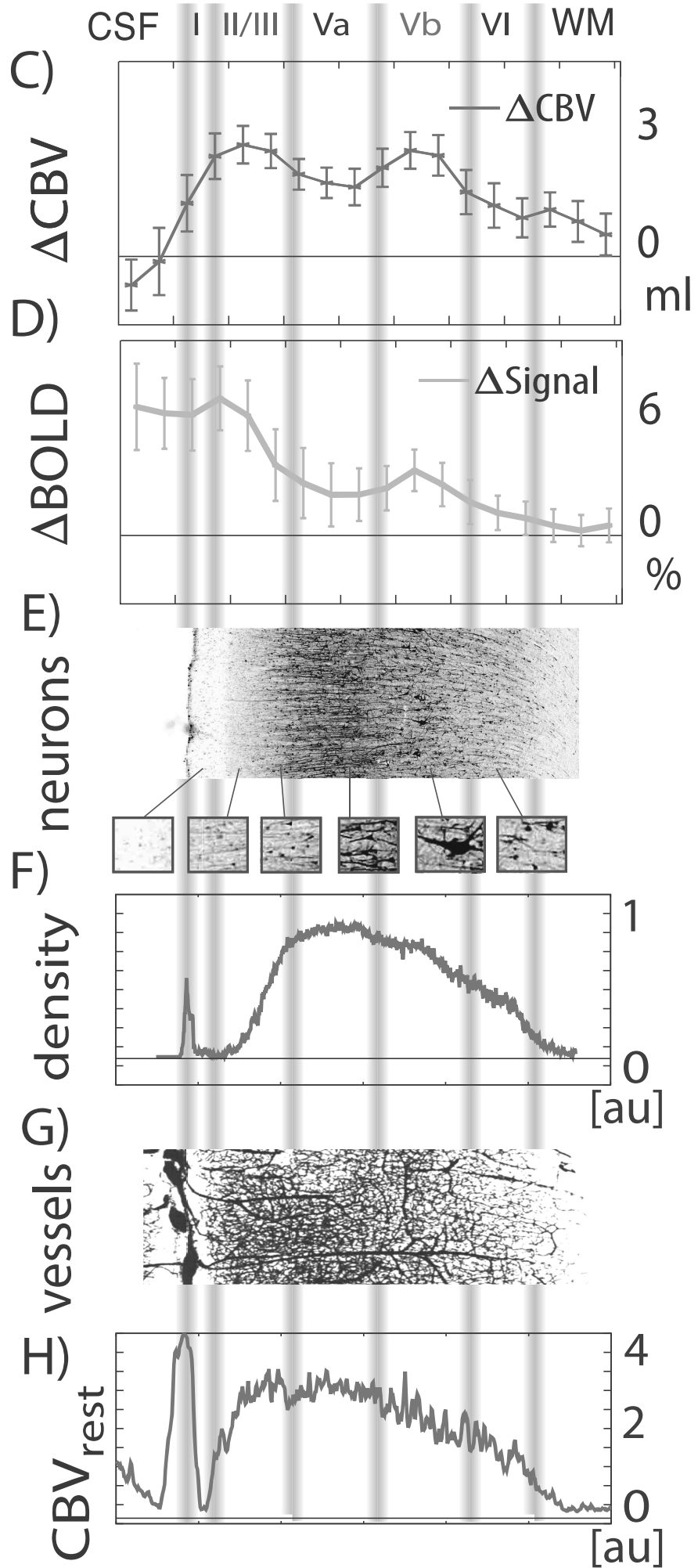
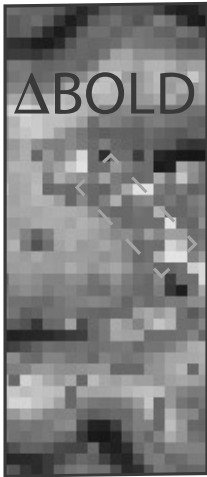


Fig. 6

A)



B)



## 10. Supplementary Material

[Click here to download 10. Supplementary Material: ManuscriptBody.pdf](#)